

ABSTRACT

OMAN, KYLE GLENN. Damage Assessment of an Integrally Stiffened Composite Panel through Dynamic Interrogation of Multiplexed Fiber Bragg Grating Sensors. (Under the direction of Dr. Kara J. Peters).

The outcome of this work was the demonstration of the measurement of dynamic responses in a complex, integrally stiffened composite panel using surface mounted FBGs. The measurements were performed using full-spectral interrogation to eliminate peak wavelength errors due to spectral distortion and will be used as benchmark data for comparison with embedded FBG sensor measurements at a later date. To obtain these measurements, several research accomplishments were achieved.

The development of a VARTM manufacturing process for high quality, integrally stiffened panel specimens was successful. Through many trial-and-error attempts, a process for manufacturing an integrally stiffened panel was laid out. In a parallel project, the same procedure was followed by another researcher to produce an integrally stiffened panel of similar dimensions and quality. The development of a numerical model to simulate the undamaged specimen was also successful. The model fit to the specimen was assessed by the correlation of experimental natural frequencies to those found through simulation. Eight of the eleven first natural frequencies found experimentally were identified closely by the numerical model, with the differences in results being accounted for by mode shape capture issues. This correlation in natural frequencies through the first 11 modes offered cleared evidence of a well-fit model and the high quality of the specimen fabrication. The applied boundary conditions damped out some natural frequencies more than others, however this is expected with physical systems.

Using a high speed, full spectral interrogator, the FBG sensors were able to clearly depict the transient response of the integrally stiffened panel subjected to harmonic excitation. Additionally, the surface mounted FBG sensors demonstrated an ability to sense minor changes in the transient response, and identified several trends that may be indicative of non-linear response in the specimen. Though these trends were not extremely strong, they do offer promising results for the potential use of FBG sensors as real-time structural health monitoring devices in aircraft. The limited sensitivity of the sensors to the changes in transient response may be a result of surface mounting the sensors. If the sensors were embedded within the carbon fiber panel, they would likely be much more sensitive to these changes and potentially offer more distinct indications of a transition to non-linear response in the panel. It should also be noted that while not the focus of this work, the dynamic response of multiple multiplexed FBG sensors were measured through high-speed, full-spectral interrogation for the first time.

The simulation of damage in the specimen offered mixed results. While the limited change in transient response as damaged was applied did support the only minor changes seen in the experimental results, it was expected to see more evolution in the transient response. Exploring the theory that the initial damage regions identified by the Micro-CT scan were conservative, the follow-up simulation using larger expected damage regions showed much greater change in the transient response of the simulated panel, though the appearance of harmonics was still notably absent. It is believed that the perfect nature of the model and the applied boundary conditions limited the appearance of these harmonic components.

© Copyright 2014 Kyle Glenn Oman

All Rights Reserved

Damage Assessment of an Integrally Stiffened Composite Panel through Dynamic
Interrogation of Multiplexed Fiber Bragg Grating Sensors

by
Kyle Glenn Oman

A thesis submitted to the Graduate Faculty of
North Carolina State University
in partial fulfillment of the
requirements for the degree of
Master of Science

Aerospace Engineering

Raleigh, North Carolina

2014

APPROVED BY:

Dr. Eric Klang

Dr. Scott Ferguson

Dr. Kara Peters
Committee Chair

BIOGRAPHY

Kyle Oman was born and raised in Kannapolis, North Carolina. He attended North Carolina State University and graduated as Valedictorian with Suma Cum Laude honors for the degree of Bachelor of Science in Mechanical Engineering in 2008. Oman was a member of the University's Caldwell Fellowship program which focused on the development of individuals as servant-leaders. He also volunteered as a tutor for local middle students in science and math, and was an active member of the NC State club soccer team.

ACKNOWLEDGMENTS

I would like to first and foremost thank my advisor, Dr. Kara Peters, for her support through the duration of my research. Her passion for the subject and enthusiasm for helping graduate students played a big role in the completion of this research.

I'd also like to thank the other members of the Smart Composites Research Lab, William Stewart, Xianyu Wu, Drew Hackney, Gary Martin, Clint Shook, and Bram Van Hoe for their help and support with various research aspects along the way. Sean Webb, a former lab member, deserves particular appreciation for teaching me how to use the lab's interrogation system.

There are also several people not affiliated with the Lab that deserve appreciation for the role they played in the completion of this work: Karim Aly for his knowledge and support in developing the VARTM process, Nikola Stan for his expertise on the high-speed interrogator, and Jimmy Thostenson from the SMiF group at Duke University for his support in performing micro-CT scanning.

I would also like to thank my committee members, including Dr. Kara Peters, Dr. Scott Ferguson, and Dr. Eric Klang, for their willingness to review my work and provide helpful feedback. Additionally, I would like to thank funding for my salary from IFOS as a subcontract to NASA Contract Number NNX12CB01C.

Lastly, I would like to thank my family and friends for their love and support through the duration of this research. The completion of this thesis would not have been possible without their encouragement.

TABLE OF CONTENTS

LIST OF TABLES	vi
LIST OF FIGURES	vii
CHAPTER 1 - INTRODUCTION.....	1
1.1 FBG SENSORS	1
1.2 FBG SENSING RESEARCH	3
CHAPTER 2 – SPECIMEN PREPARATION	8
2.1 STIFFENED PANELS	8
2.2 SPECIMEN DESIGN	9
2.3 MANUFACUTRING PROCESS	11
2.3.1 TRIAL 1.....	13
2.3.2 TRIAL2.....	15
2.3.3 TRIAL 3.....	17
2.3.4 TRIAL 4.....	20
2.3.5 TRIAL 5.....	21
2.4 FINAL SPECIMEN SPECIFICATIONS.....	22
CHAPTER 3 – MODEL DEVELOPMENT.....	24
3.1 NUMERICAL MODEL GEOMETRY.....	24
3.2 NUMERICAL MODEL PROPERTIES.....	30
CHAPTER 4 – EXPERIMENTAL TESTING	34
4.1 NATURAL FREQUENCY TESTING.....	34
4.2 MODEL FITTING.....	43
4.3 VIBRATION AND IMPACT DATA COLLECTION	49
4.4 VIBRATION AND IMPACT TEST RESULTS	65
CHAPTER 5 – SIMULATIONS.....	82
5.1 MODELING DAMAGE.....	82
5.2 TRANSIENT FORCE APPLICATION	83
5.3 MODEL SIMULATION RESULTS	86
CHAPTER 7 - CONCLUSION.....	92
7.1 CONSLUSIONS.....	92
7.2 FUTURE WORK	94

REFERENCES	95
APPENDICES	97
APPENDIX A – VARTM PROCESS	98

LIST OF TABLES

Table 1: Model material properties.....	30
Table 2: Tensile testing coupon specifications.....	31
Table 3: Modulus estimations based on slope of elastic region of stress vs. strain curves. ...	33
Table 4: Measured specimen natural frequencies. All values are in Hz.....	42
Table 5: Natural frequencies calculated through finite element model.....	45
Table 6: Comparison of natural frequency results. Mode numbers are taken from finite element model.....	45
Table 7: FBG sensor labels and corresponding Bragg wavelengths.....	50

LIST OF FIGURES

Figure 1.1: Fiber Bragg grating spectral response to broadband input spectrum.	2
Figure 1.2: FBG spectral response to tension and compression [1].	2
Figure 1.3: Spectral response of FBG sensors in the Takeda study [3].	4
Figure 1.4: (a) Single full-spectral scan at $t=t_0$, (b) dynamic full-spectral scanning for some time period, and (c) 2D false-color mapping. Intensity axis is replaced with a color scale.....	5
Figure 2.1: Traditional stiffened panel geometry.	8
Figure 2.2: Nominal specimen dimensions (mm).	10
Figure 2.3: Individual dry fiber section dimensions. Skin section is shown on left; stiffener section is shown on right.....	10
Figure 2.4: Section location during VARTM process.	11
Figure 2.5: Section stacking sequence. Shading lines show fiber orientation.	11
Figure 2.6: Typical VARTM assembly.	12
Figure 2.7: (a) Trial one under vacuum pressure; (b) Final specimen from trial one.	13
Figure 2.8: (a) Trial two under vacuum pressure; (b) Final specimen from trial two.	15
Figure 2.9: (a) Trial three under vacuum pressure; (b) Final specimen from trial three.	17
Figure 2.10: Layup Cross Section for Trial 3	18
Figure 2.11: (a) Trial four under vacuum pressure; (b) Final specimen from trial four.	20
Figure 2.12: Layup Cross Section for Trial 4	20
Figure 2.13: (a) Trial five under vacuum pressure; (b) Final specimen from trial five.	21
Figure 2.14: Final specimen dimensions (mm).	23
Figure 3.1: Base model geometry.	25
Figure 3.2: (a) Area thicknesses; (b) detail view of stringer base.	26
Figure 3.3: Stringer-plate interface options: (a) one and (b) two.	26
Figure 3.4: 8 Layer stacking sequence for the numerical model.	28
Figure 3.5: (a) Complete model display; (b) end-view of model; (c) stringer hollow-cavity detail; and (d) detail view of element layers.	29
Figure 3.6: Final ANSYS model.....	30
Figure 3.7: Stress vs. Strain for (a) specimen 1; and (b) specimen 4. Elastic regions boxed in red.	32
Figure 4.1: Stiffened panel specimen mounted on vibration platform.	34
Figure 4.2: Vibration table components.....	36
Figure 4.3: Accelerometer Mounting Locations.....	37
Figure 4.4: Voltage vs. time data at 100 Hz and accelerometer location 1.	38
Figure 4.5: Frequency response at 100 Hz and accelerometer location 1.	39
Figure 4.6: Frequency response curve for vibration table and mounting system.	40
Figure 4.7: Frequency response curves for the specimen at accelerometer locations (a) one, (b) two, and (c) three (see Figure 4.3).	42
Figure 4.8: Model boundary conditions.....	44
Figure 4.9: Calculated mode shape of mode 7 and accelerometer locations.	47
Figure 4.10: (a) Mounted FBG sensors on stiffened panel and (b) detailed view of sensors.	50

Figure 4.11: FBG locations. All dimensions in mm.	51
Figure 4.12: Stiffened panel mounted for impact testing.	52
Figure 4.13: Impact locations, skin-side of panel. All dimensions in mm.	53
Figure 4.14: Detailed view of impacts: Impact 1 (a) skin side and (b) stiffener side; Impact 2 (c) skin side and (d) stiffener side; Impact 3 (e) skin side and (f) stiffener side; and Impact 4 (g) skin side and (h) stiffener side.	54
Figure 4.15: CT scan of impact locations (a) 1, (b) 3, and (c) 4. All dimensions in mm.	58
Figure 4.16: CT Scan of impact 2 (a) progressive damage and (b) detailed view of damage. All dimensions in mm.	59
Figure 4.17: (a) Block diagram and (b) photograph of FBG full-spectral interrogator	62
Figure 4.18: ASE-EDFA output intensity spectrum.	63
Figure 4.19: (a) Reflection spectrum and (b) time response of mounted FBG sensors on the undamaged, non-vibrating specimen. In (b), the colorscale corresponds to reflected intensity with red as maximum intensity.	63
Figure 4.20: Wavelength spectrums for impacts (a) one, (b) two, (c) three, and (d) four.	64
Figure 4.21: Dynamic response of FBG sensors to 150 Hz excitation: (a) undamaged, (b) post-impact 1, (c) post-impact 2, (d) post-impact 3, and (e) post-impact 4.	66
Figure 4.22: Strain data for FBGs (a) A, (b) B, (c) C, and (d) D for the undamaged specimen excited at 150 Hz.	70
Figure 4.23: FFT results for FBGs (a) A, (b) B, (c) C, and (d) D for the undamaged specimen excited at 150 Hz.	70
Figure 4.24: (a) Raw STFT data showing Hamming windows and (b) contoured STFT data for FBG B on the undamaged specimen excited at 150 Hz.	72
Figure 4.25: Contoured STFT data for FBG A (A) and FBG B (B) when (0) undamaged, and after (1) impact 1, (2) impact 2, (3) impact 3 and (4) impact 4. All data are at 150 Hz excitation frequency.	73
Figure 4.26: Contoured STFT data for FBG C (C) and FBG D (D) when (0) undamaged, and after (1) impact 1, (2) impact 2, (3) impact 3 and (4) impact 4. All data are at 150 Hz excitation frequency.	76
Figure 4.27: Contour plot for FBG B after impact 4, with color scale mapped to the max value on the plot.	80
Figure 5.1: Damage (green) and FBG (yellow) locations within the FEA model for the (a) whole model and in (b) a detailed view.	83
Figure 5.2: (a) Force vs. time plot for vibration table transient force and (b) associated FFT plot.	85
Figure 5.3: Sum of sines fit for transient input force.	85
Figure 5.4: Loading case for simulated harmonic excitation.	86
Figure 5.5: (a) Undamaged model, (b) model with damage shape based on micro-CT scans, and (c) model with expected damage regions. Green area is damage region.	89
Figure 5.6: STFT for model results. (a) Left column is undamaged case, (b) middle is micro- CT scan damage shape case, and (c) right is expected damage case. Note intensity scales vary.	90

Figure 5.7: FFT for model results. (a) Left column is undamaged case, (b) middle is micro-CT scan damage shape case, and (c) right is expected damage case.	91
Figure A.1: Completed VARTM assembly.	98
Figure A.2: Stiffener layup.	98
Figure A.3: Stiffener clamping procedure.	100
Figure A.4: Completed stiffener mold.	100
Figure A.5: Cross-section of mold lay up.	102
Figure A.6: Vacuum seal spacing.	103
Figure A.7: Inlet/outlet tube connection diagram.	103
Figure A.8: Inlet/outlet tube vacuum seal.	104
Figure A.9: Vacuum seal layout.	105
Figure A.10: Initial vacuum seal around inlet/outlet tubes.	106
Figure A.11: Final vacuum seal around inlet/outlet tubes.	106
Figure A.12: Crimping procedure for vacuum seal.	107
Figure A.13: Peel ply used for removing stiffener molds.	109
Figure A.14: Putty knife used to remove stiffener molds.	110

CHAPTER 1 - INTRODUCTION

1.1 FBG SENSORS

The growth of carbon fiber's use in the aerospace industry presents new challenges in assessing the structural health of aerospace structures. Traditional aluminum structures show damage clearly, both on the impact surface and the reverse side. Carbon fiber structures, however, will often appear fine on the surface, but be damaged internally or on the reverse side. With planes like Boeing's 787 being comprised of over 50% advanced composite materials, it becomes critical to be able to accurately assess the structural integrity of carbon fiber structures. One promising area of research is fiber Bragg grating (FBG) sensors.

A fiber Bragg grating is a type of distributed Bragg reflector that is inscribed within a short segment of optical fiber. This reflector will only reflect particular wavelengths of light, while transmitting all others. If a broadband light source is input to a fiber Bragg grating, most of the broadband light will be transmitted, while a particular portion of the light will be reflected; the portion of light reflected is known as the Bragg wavelength (λ_B) of FBG.

Figure 1.1 depicts this transmission and reflection concept. By tracking the changes in this reflected light, it is possible to use an FBG as a sensor. As shown in Figure 1.2, as λ_B shifts right (increase in wavelength), the sensor is in tension. As λ_B shifts left (decrease in wavelength), the sensor is in compression. The wavelength shift, $\Delta\lambda_B$, is related linearly to the strain acting on the sensor by the equation

$$\varepsilon = \frac{\Delta\lambda_B}{\lambda_{B_0}(1 - p_e)} \quad (1)$$

where $\Delta\lambda_B$ is the wavelength shift, λ_{B_0} is the initial wavelength, and p_e is the strain optic coefficient of the sensor material. If the FBG is fixed to a specimen, this relationship can be exploited to allow the FBG to be used as a local strain sensor.

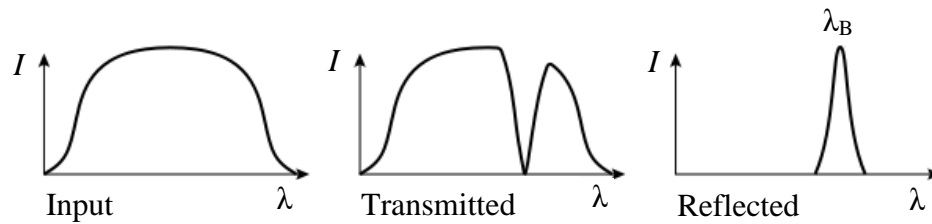


Figure 1.1: Fiber Bragg grating spectral response to broadband input spectrum.

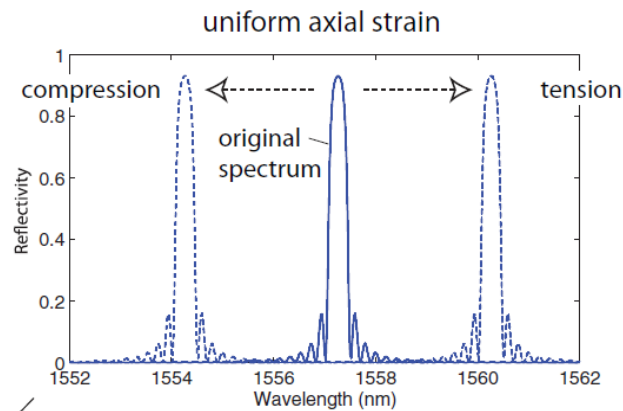


Figure 1.2: FBG spectral response to tension and compression [1].

The manner in which an FBG is fixed to a specimen affects how well a specimen transfers strain to the sensor. While FBGs can be surface mounted to materials using standard strain gauge glue, when working with composite materials, they can also be embedded within

the composite layup. These integrated sensors provide better strain transmission from the specimen to the sensor, but the methods for integrating these sensors effectively is a subject of current research. Embedding sensors in the material runs the risk of damaging the sensor, in addition to having minor effects on the local integrity of the final specimen.

Despite these challenges, using FBGs as strain sensors still has many advantages over the classic electrical resistance strain gauge, including:

- Several sensors can be multiplexed into a single optical fiber (avoids the wiring problems of using multiple electrical resistance strain gauges)
- FBGs are extremely small
- FBG sensors can be embedded within structures
- FBGs work over long distances of fiber cable (kilometers)
- FBGs are naturally immune to electromagnetic interference

1.2 FBG SENSING RESEARCH

The capabilities of Fiber Bragg Gratings as structural health sensors for composite structures have been well documented [2], and the technology has developed to a point where peak tracking FBG interrogation systems are commercially available. Current research focuses on pushing FBG technology further, and gleaning as much information as possible from the instrumentation. One area of particular interest is in pursuing full-spectral information during FBG interrogation, rather than simple peak tracking. In the work by Takeda *et al* [3], full-spectral interrogation was performed on two FBGs (FBG-A and FBG-B), embedded within a stiffened panel, after an impact event occurred. These FBGs were

embedded within the adhesive layer between the stiffener and skin of the stiffened panel, and the impacts were applied on the skin-side of the panel. Figure 1.3 displays the spectral response of each FBG before and after the impact occurs.

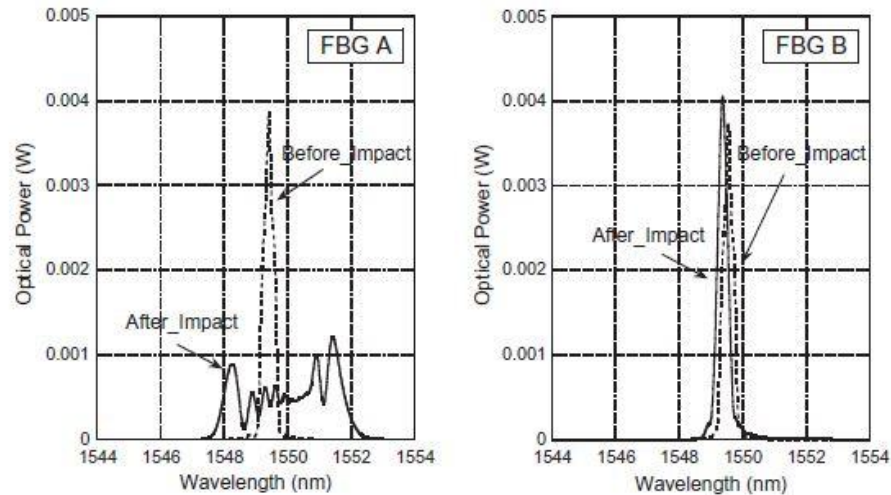


Figure 1.3: Spectral response of FBG sensors in the Takeda study [3].

The results of this study demonstrated clearly that the resulting strain from impact events could be captured by full spectral interrogation of FBG sensors. Additionally, the study highlights the advantages of full-spectral interrogation over peak tracking. In Figure 1.3, the response of FBG A after the impact is a severely distorted signal. While the peak tracking method would merely identify the peak with the greatest power and only see a shift in wavelength to this point, the full-spectral interrogation shows fully the distortions that offer more information about the strain in the specimen. The utilization of this full spectral information has the potential to give more information regarding the failure modes of the carbon structures.

In the interest of capturing full-spectral information for impact events as they occur, research has been performed into increasing the rate of data acquisition from FBG sensors by Vella *et al* [4]. To achieve this, the authors developed a high speed, full-spectral interrogator that is capable of recording full-spectral data at rates up to 300 kHz, as opposed to the commercially available scanners that can reach only ~ 1 kHz scan speeds. This interrogator is also used in the current study, and details are discussed at a later point.

The research performed by Vella required displaying the response of FBG sensors over time. To do so, the authors developed a method called 2D false-color mapping to show these results. This technique utilizes a color scale to depict the intensity of light at a particular wavelength and time, as overviewed in Figure 1.4. Under this method, individual full-spectral sweeps are taken (Figure 1.4(a)) and stacked back-to-back over time (Figure 1.4(b)). The intensities of this spectrum are then replaced with a color-scale, allowing it to be viewed in two-dimensions (Figure 1.4(c)).

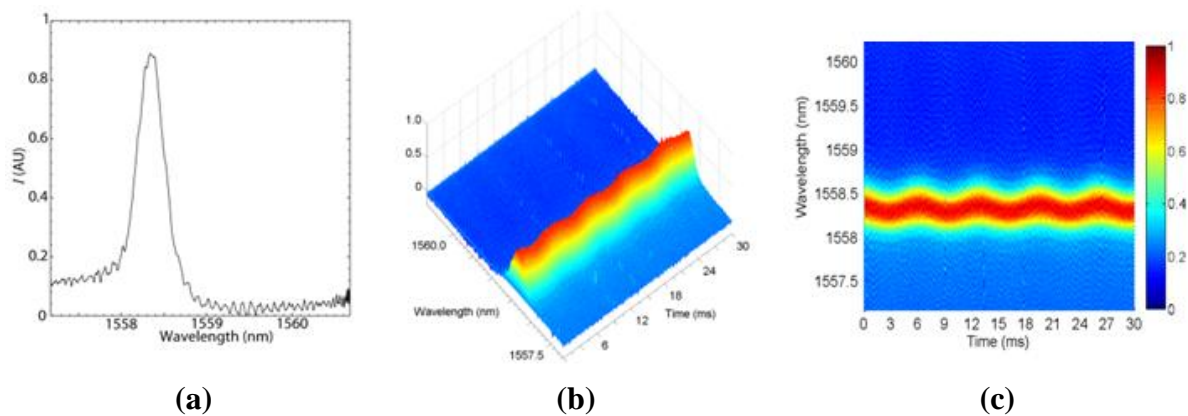


Figure 1.4: (a) Single full-spectral scan at $t=t_0$, (b) dynamic full-spectral scanning for some time period, and (c) 2D false-color mapping. Intensity axis is replaced with a color scale.

Given the ability to embed FBG sensors within composite structures, there is also interest in how the sensors would fair in real-world environments. As noted previously, aircraft are making increasing use of carbon fiber, and are prime candidates for the structural health monitoring capabilities of FBG sensors. Given this potential application, research is also being performed into the effects of aircraft vibration on FBG sensor capabilities. Initial research demonstrated that FBG sensors embedded in carbon fiber that was exposed to steady-state vibration were still capable of producing accurate full-spectral information after filtering out noise due to the vibration [5]. Further research aimed to investigate the effects of fatigue damage on aircraft lap joints subjected to the same simulated aircraft vibration [6, 7]. In this work, FBG sensors were embedded within the adhesive layer of lap joints, which were then subjected to fatigue loading. These lap joints were then subjected to harmonic oscillation simulating aircraft vibration, while the FBG sensors were interrogated at regular intervals. The FBG sensors showed a transition from linear to non-linear response in the joint as the damage increased. This result serves as a first step in verifying the viability of embedding FBG sensors in aircraft structures for health monitoring purposes. Further research is necessary to conclusively deem FBG sensors as a viable option for aircraft structural health monitoring needs, and furthering this work will be the focus of this study.

Previous work focused on the interrogation of single FBG sensors, mounted to simple structures or embedded within the adhesive layers between composite panels. This study aims to push this technology further by utilizing the multiplexing ability of FBGs to interrogate several FBG sensors at once. Additionally, these FBG sensors will be applied to a

complex aerospace structure to assess their reliability during aircraft vibration. In summary, the goals of this study will be as follows:

1. Manufacturing of a high quality integrally stiffened panel.
2. Mounting multiplexed FBG sensors to the composite structure and experimentally measuring the transient response.
3. Development of a numerical model to simulate the manufactured specimen and verify its predictions of transient response.

CHAPTER 2 – SPECIMEN PREPARATION

2.1 STIFFENED PANELS

The research outlined above focused on composite specimens that consisted of several individual composite pieces bonded together with adhesives; this research will focus on an emerging technology for aerospace composites: integrally stiffened panels. These panels will offer a significantly more complex dynamic environment in which the sensors must operate. A traditional stiffened panel is shown in Figure 2.1.

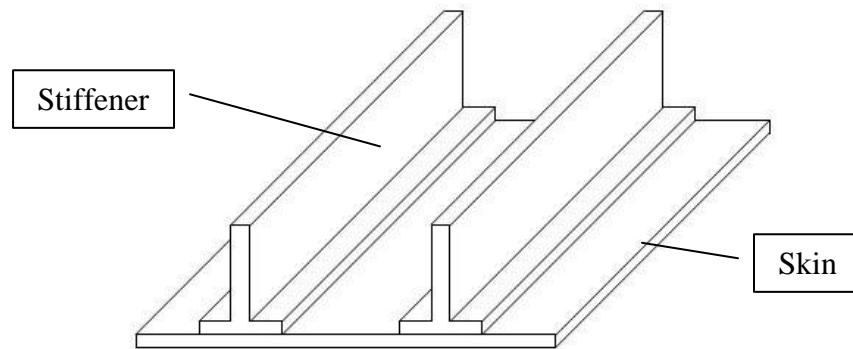


Figure 2.1: Traditional stiffened panel geometry.

A stiffened panel consists of a flat panel or skin reinforced with stiffeners, most often T-shaped. In traditional aluminum structures and composite structures, these panels and stiffeners are manufactured separately, and then connected using rivets or adhesives, respectively. However, composites research has led to the development of a new fabrication

technique: the integrally stiffened panel. Stiffeners that are integrally cured with the skin panel offer the following advantages [8]:

1. Large one-piece structures can be made, eliminating joints and discontinuities, and improving structural integrity.
2. The manufacturing process involves fewer operations.
3. Fewer fit problems occur, and less sealing is required in assemblies.

2.2 SPECIMEN DESIGN

The specific dimensions and design of the specimen were based on previous work using FBGs to monitor stiffened panels [3]. The goal was to produce a specimen that had realistic dimensions, and would appropriately represent a real aircraft component. The fiber utilized for production of the panel is unidirectional carbon fiber, with a weight of 125 g/m^2 and a thickness of 0.229 mm [9]. The epoxy used is System 2000 epoxy and 2120 Epoxy Hardener produced by Fibre Glast Developments Corporation. The 2120 hardener gives a pot life of 120 minutes to the resin, allowing ample time to complete the resin infusion process. Figure 2.2 displays the nominal specimen dimensions. To achieve this shape, the specimen was assembled using 5 sections of dry fiber: a large flat section for the skin, and 2 pairs of narrow sections for the stiffeners. Figure 2.3 shows these section dimensions and Figure 2.4 shows how the sections are placed in relation to each other when placed within the resin infusion setup.

Each section consists of 8 layers of unidirectional carbon fiber. The specific stacking sequence for all sections used is $[+45^\circ/-45^\circ/0^\circ/90^\circ]_S$, where 0° corresponds to the X-direction in the coordinate system shown in Figure 2.3. This stacking sequence provides a symmetric layup, therefore eliminating warping of the structure during cure, while strengthening the skin and stiffeners in multiple directions. Following this system, Figure 2.5 shows the different layers of each section.

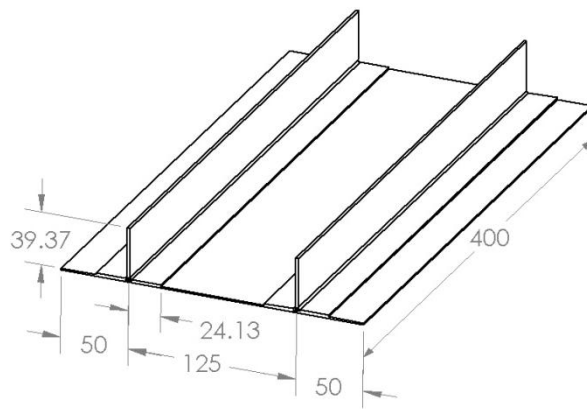


Figure 2.2: Nominal specimen dimensions (mm).

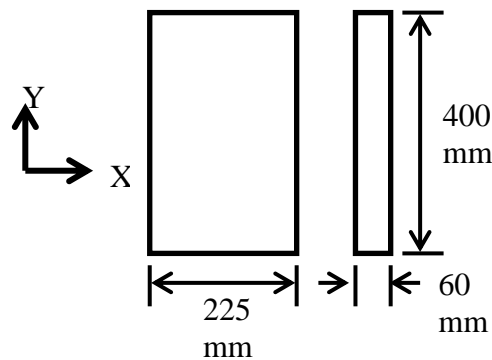


Figure 2.3: Individual dry fiber section dimensions. Skin section is shown on left; stiffener section is shown on right.



Figure 2.4: Section location during VARTM process.

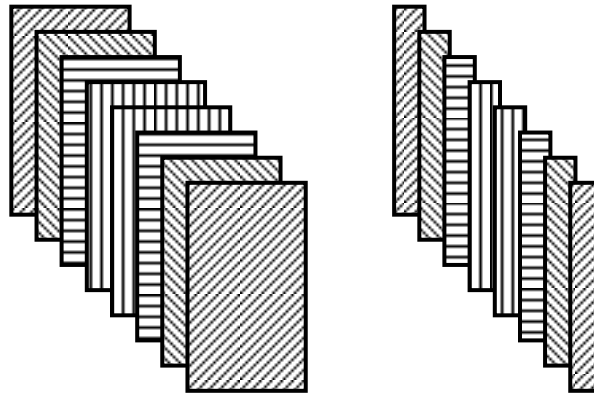


Figure 2.5: Section stacking sequence. Shading lines show fiber orientation.

2.3 MANUFACTURING PROCESS

Vacuum assisted resin transfer molding (VARTM) was used to create the integrally stiffened panel. The VARTM process involves placing dry fiber fabric on a mold and enclosing the mold within a vacuum bag. The resin is then drawn into the vacuum through an inlet, pulled through the dry fabric on the mold, and then pulled out of the mold through an outlet. This method allows for the creation of complex geometries, as is the case for a stiffened panel, because the vacuum bag can stretch to fit the shape of the mold. Figure 2.6 displays a cross section of a typical VARTM assembly.

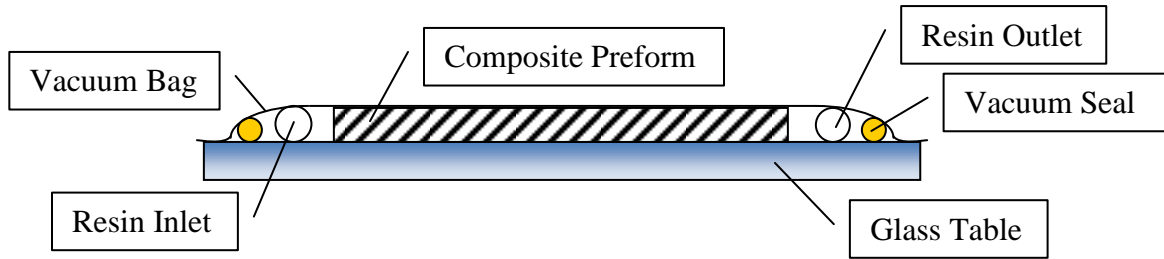


Figure 2.6: Typical VARTM assembly.

Figure 2.6 displays a flat panel of composite material, but if proper molds are created, it is possible to create a complex geometry. The resulting specimen will consist of purely fiber and resin, avoiding the need for any fasteners or adhesives.

Although the general steps of the VARTM process are well known, the details of the process are proprietary information at most companies; the parameters and procedures must be tuned to the particular fiber, resin, cure cycle used and the geometry of the specimen. The following section will therefore discuss the various trials performed attempting to produce the specified specimen using the VARTM process. An image of the trial setup and result is given at the start of each trial discussion.

2.3.1 TRIAL 1



Figure 2.7: (a) Trial one under vacuum pressure; (b) Final specimen from trial one.

The initial trial for the production of an integrally stiffened panel is shown in Figure 2.7. In this trial, there was a single stiffener formed by foam molds. These molds were created by running a current through a metal wire and using this wire to cut the foam. The molds were coated with 2 layers of car wax and placed directly against the carbon fiber sheet. Peel ply was placed on all other exposed carbon surfaces. The resin inlet and outlet were located on the ends of the stiffener. The vacuum bag used in this trial was Stretchlon 200 Bagging Film.

The manufacturing of the foam molds themselves proved to be difficult. Although the hot-wire cutting method was effective for cutting the foam, because of the length of these molds (about 41 cm) there were problems with getting consistent cuts. The wire would often “lag” in the middle of the mold (meaning the outside edges traveled faster than the middle section) leading to non-uniform cuts.

There were also challenges in creating a sealed vacuum environment. Although these images represent the first resin infusion trial, it actually took three attempts to create a sealed vacuum environment in which to perform the infusion. Typically, most leaks in the vacuum could be found audibly. However, even when there were no audible leaks, the pressure in the bag would slowly decrease. It is believed that the thin nature of the vacuum bag was allowing micro-tears to develop in areas of high stress (such as the corners of the mold).

There were also problems with the actual infusion process. First of all, there were many air bubbles present in the resin. These air bubbles would likely lead to defects in a completed infusion. Secondly, the rate of resin travel through the preform was much too slow. The epoxy and hardener used (System 2000 epoxy and 2120 Hardener) allow for 2 hours of infusion time. At 2 hours, the resin had progressed through less than 50% of the preform. This means the resin viscosity was rapidly increasing, thus making it even harder for the resin to finish covering the preform. The specimen was found to be only about 50% covered with resin after being allowed to cure. The stiffener was found to be particularly dry.

Lastly, when trying to remove the foam molds, it was found that the resin had bonded to the foam, making them difficult to remove. This was particularly a problem near the inlet, where resin had actually seeped into the semi-porous foam, making it nearly solid and impossible to remove.

2.3.2 TRIAL2

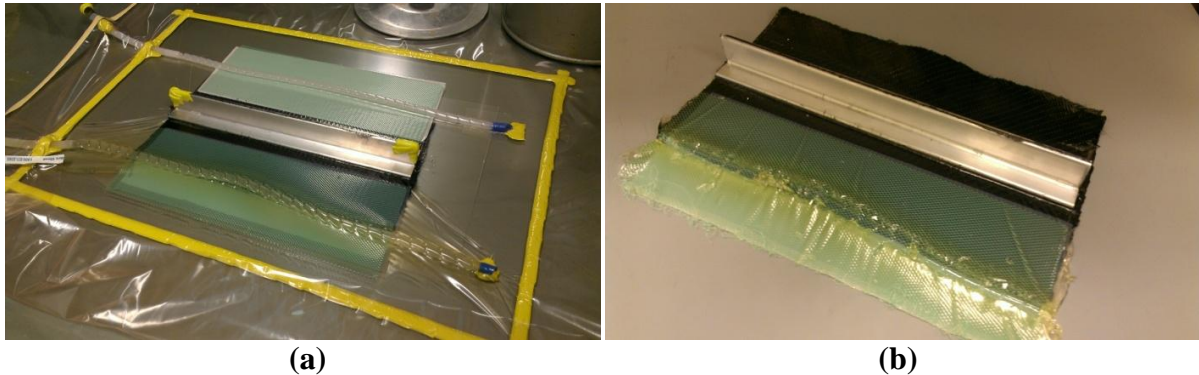


Figure 2.8: (a) Trial two under vacuum pressure; (b) Final specimen from trial two.

Several major changes were made in the second infusion trial. The first change was to use aluminum molds instead of foam, as can be seen in Figure 2.8. These molds are not porous and thus will not absorb any resin and theoretically be easier to remove. The inside surfaces of these molds were coated with 2 layers of car wax and a layer of peel ply was placed between the mold and the carbon to help facilitate the removal process.

The second change was in the orientation of the inlet and outlet tubes. Instead of being placed on the ends of the panel, they were placed on the sides, as shown in Figure 2.8. With this orientation, the resin would be forced to travel through the stiffener (rather than beside it, as in the other orientation) and hopefully travel up into the stiffener. The third change was to add resin flow media near the resin inlet in order to speed up the infusion rate. Including this flow media would allow the resin to travel faster across the preform surface. The goal was to keep make the resin travel quickly to the stiffener.

The fourth change was in the vacuum bag used. A thicker bag (Stretchlon 800 Bagging Film) was selected with the aim of avoiding the micro-tearing experienced in the previous trial. The fifth major change was to include a de-gassing phase in the preparation of the epoxy. After mixing the epoxy and hardener, the mixture was placed in a vacuum chamber for 30 minutes to remove any air bubbles present in the resin.

There were three main problems found during this trial. The first two relate to the resin flow rate. Although the addition of flow media did increase the speed of the resin flow rate near the inlet, the flow rate was still extremely slow everywhere else. When the resin reached the end of the flow media, the flow speed drastically decreased. This rate of infusion was still too slow to cover the entire preform within the allotted 2 hour working time. When removed, the preform was approximately 75% coated in resin, with the dry area being in the flat panel near the outlet. This change in flow rate also caused problems at the inlet. The point where the flow media ended and the flow rate drastically decreased acted like a wall, blocking the resin from traveling. As resin continued to pour in from the inlet at an accelerated rate, it was continually blocked by the slower flow rate where the flow media ended. This caused a significant resin buildup around the inlet tube. When removed from the vacuum environment, it was impossible to separate this resin build up from the preform structure.

The third major problem was that the aluminum molds could not be removed. This problem was attributed to two areas. The first was the resin build up. The large amounts of resin pooling near the mold allowed excess resin to gather under the mold and to settle on top of the mold, making it harder to remove. The second issue was the inability to reach the peel

ply. Because the peel ply was cut the same size as the mold, there was no peel ply exposed to be used to peel off the molds; it was simply glued between the mold and preform.

2.3.3 TRIAL 3

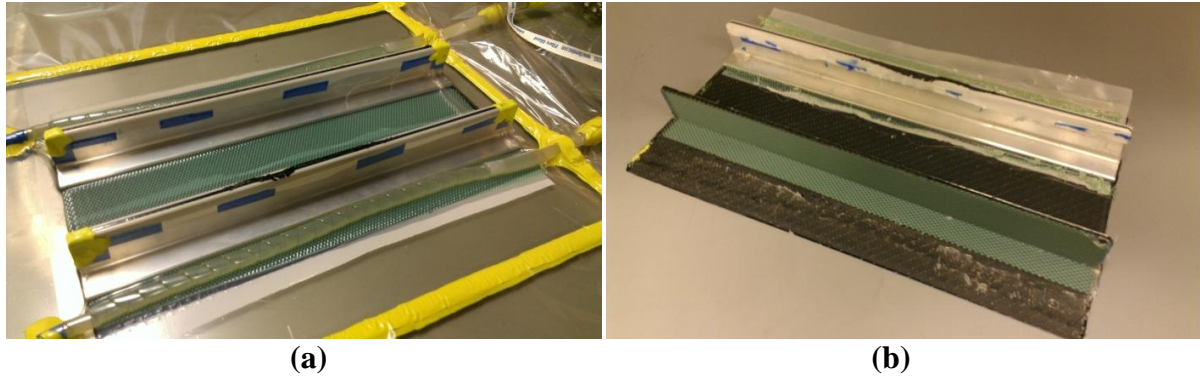


Figure 2.9: (a) Trial three under vacuum pressure; (b) Final specimen from trial three.

The main goal of trial 3 was to have 100% of the preform coated in resin. To achieve this, all surfaces were covered with flow media. As shown in Figure 2.9, two stiffeners were used in this trial instead of one because of the nature of the trial. Knowing that 2 stiffeners were desired in the end, it made sense to go ahead and test 2 stiffeners with flow media everywhere to verify that the flow rate could be increased enough to coat the entire specimen. The exposed areas of panel around the stiffeners had a single layer of flow media placed over the peel ply (same as the area around the inlet in the previous trial). The stiffeners themselves were also given a layer of flow media. This flow media was placed between two layers of peel ply, which was then between the carbon and the mold.

Another significant change in this trial was how the peel ply was applied. Rather than cutting strips to fit in the molds and separate strips to cover the exposed panel regions, the

peel ply inside the molds was cut long enough that it extended out from the molds and covered the exposed panel with a single piece. There was also a small tab of peel ply left protruding from the top of the molds (which was then taped down to the sides of the molds, as seen in Figures 2.9 and 2.10). See Figure 2.10 for a cross section of the layup. Note that there was also tape added around the ends of the molds. This was done to help hold the molds tightly together before the vacuum was applied.

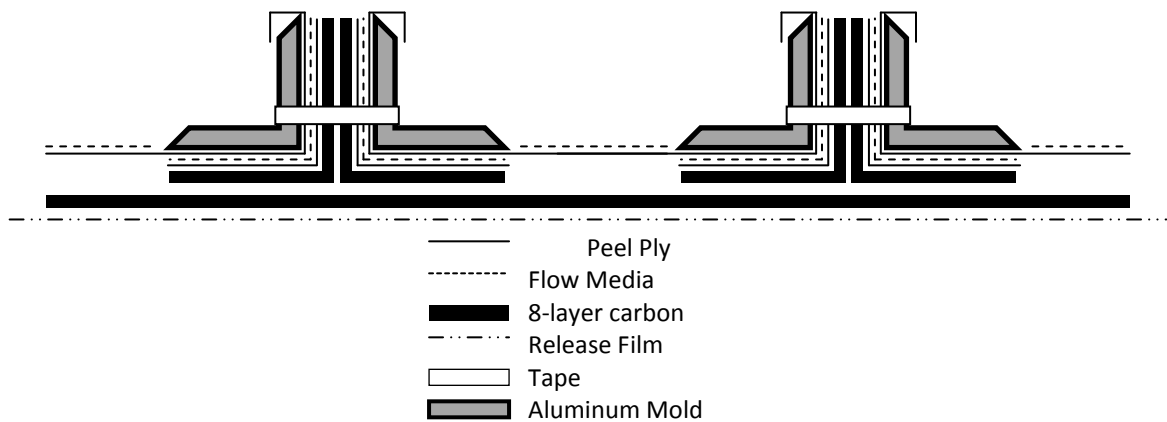


Figure 2.10: Layup Cross Section for Trial 3

During the vacuum bagging processes, it was found that the molds could not be located too closely to the edges of the vacuum seal or the bag could not adequately form to the shape of the mold. When placed too closely, the vacuum bag would form folds or wrinkles extending down from the top of the molds (this can be seen in Figure 2.9(a) above). These create channels that could lead to air leakage problems that are difficult to seal, or create undesired channels for resin to flow through. To mitigate this problem, it was

determined that a minimum of 6 cm should be left between the preform and the vacuum seal at the ends of the mold, and around 3 cm on the sides.

The most important result of this trial was that the entire preform was coated with resin. This was achieved well under the allotted 2 hours of working time for the resin (around 45 minutes for the entire surface to be wet). There was also significant success with removing one of the aluminum molds (the mold near the inlet could not be removed and will be addressed later). The trick to removing the mold was to wedge a putty knife between the aluminum mold and the flap of peel ply at the top corner of the molds. It was possible to then work down the length of the mold until it popped off. This exposed the large strips of peel ply that could then be peeled away, exposing most of the specimen. However, this presented a new problem. After the large sheet of peel ply was removed, it was impossible to remove the flow media that was within the stiffener molds. The peel ply beneath this flow media was unreachable because the resin had completely encapsulated both the flow media and peel ply, fusing them to the stiffener.

There was also a continued problem with the resin build up near the inlet. Again, a significant amount of resin collected around the inlet tube, causing excess resin to collect beneath and on top of the first mold. This excess resin made it impossible to remove the mold nearest the inlet without damaging the specimen.

Resin build up caused problems throughout the specimen in this trial. It was impossible to remove either mold due to the excessive resin that built up under the molds and on top of them. In this trial, the resin buildup wasn't limited to just around the inlet tube, but rather around the entire specimen. A clear reason why this buildup was so much worse than other trials could not be determined.

2.3.5 TRIAL 5

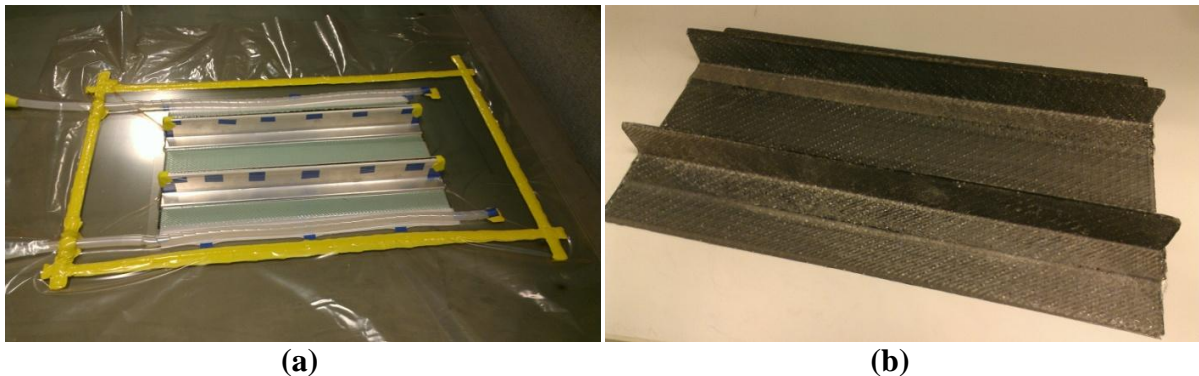


Figure 2.13: (a) Trial five under vacuum pressure; (b) Final specimen from trial five.

The layup and result for trial 5 is shown in Figure 2.13. There were 2 major changes made in this trial in order to avoid resin buildup. The first was to move the inlet and outlet tubes off of the preform. In other trials, the inlet tube was placed on top of the panel, while in this case, it is placed beside the panel. This will allow any resin that does build up around the inlet/outlet tubes to not be fused to the panel itself. In addition to move the tubing, there infusion process was also changed slightly. Once the entire specimen was coated with resin (resin flow can easily be checked visually), the inlet tube was clamped shut. This allowed the

vacuum to pull directly on the resin built up around the inlet. Once most of this buildup was pulled into the mold, the vacuum was turned off as usual.

The changes to avoid resin buildup were completely successful; when removed from the vacuum setup, there was no excessive resin buildup on the specimen. The molds were removed in the same manner discussed in trial 3, and the changes made in trial 4 were also successful. Moving the large strip of peel ply beneath all other layers made it simple to pull everything off of the carbon specimen. The comprehensive list of steps followed in trial five for the VARTM setup can be found in Appendix A.

2.4 FINAL SPECIMEN SPECIFICATIONS

The final specimen dimensions are given in Figure 2.14 below. Note that these dimensions are slightly different than the original planned dimensions of the specimen. While the length of the specimen is the same at 400 mm, the width is slightly larger at 227 mm versus the planned 225 mm. This is attributed to slight shifting of the carbon panels during the setting of the vacuum. Of more critical note is the spacing of the stiffeners; while they were planned to be spaced evenly, that clearly is not the case as shown in Figure 2.14. This was an outcome of an imprecise manufacturing process, and could be made more accurate if more attention were paid to the placement of the stiffeners during the layup process. However, perfectly uniform placement is not necessary for this testing; the planned specimen size was merely meant as a global guideline for sizing. As this specimen will be used for testing, the finite element model developed for this specimen will be built based on the actual specimen dimensions, thus alleviating any errors due to varying from the design size.

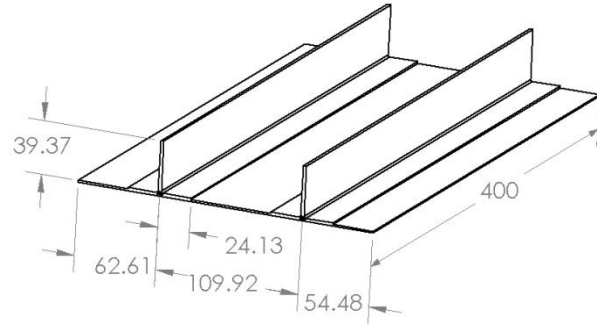


Figure 2.14: Final specimen dimensions (mm).

CHAPTER 3 – MODEL DEVELOPMENT

3.1 NUMERICAL MODEL GEOMETRY

The finite element model was developed with the intent of using it as a comparison point for the experimental FBG strain measurements. This will serve as validation for the experimental results found using the FBG sensors. In order to verify that the model predicted well the dynamic response of the pristine stiffened panel, the natural frequencies of the numerical model were calculated and compared to those measured from the experimental specimen. As not all the required material properties were known for the numerical model, an iterative process was used to fit the remaining properties through fitting of the natural frequencies under 500 Hz.

The finite element model developed for this research was created in ANSYS Mechanical APDL 14.0, though the initial model geometry was developed in SolidWorks and imported into ANSYS. The base model geometry is shown in Figure 3.1. Note that the base geometry consists of planar areas rather than solid volumes. The geometry was created in this manner because shell elements, rather than volume elements, were used to model the structural response. Shell elements provide efficient modeling of thin-walled composite structures. By using shell elements, it is possible to layer several elements together to create a solid structure. Additionally, shell elements offer significantly reduced computation time over volume elements. The specific shell element selected for this model was SHELL181. SHELL181 is suitable for analyzing thin to moderately-thick shell structures, and offers a

built in feature for modeling layered elements. This feature allows users to define aspects of individual layers of an element, including the number of layers, layer thickness, material properties, and orientation.

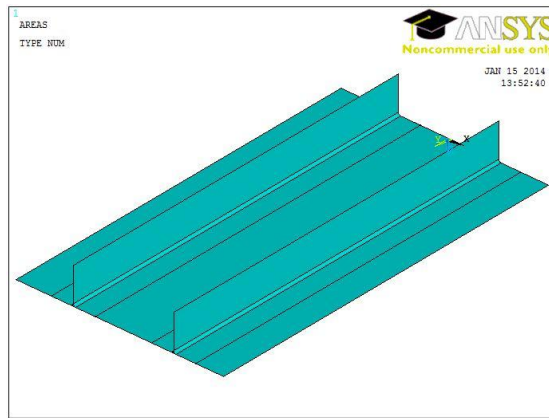


Figure 3.1: Base model geometry.

Due to the skin overlapping the stiffener as shown in Figure 2.4, the model consists of 8 layer and 16 layer sections. Figure 3.2 shows which areas are associated with each thickness; green areas are 8 layers while blue areas are 16 layers. Note that the base of the stringers was modeled with two 8 layer thick sections rather than a single 16 layer section, creating a hollow cavity at the base of the stringer. When creating the model, two options for creating this stringer-plate interface were considered, as shown in Figure 3.3.

Option one is simpler to model, however does not accurately reflect the geometry of the actual specimen. Creating the model in this manner would have created areas of stress concentration at the base of the stringer. Option two better represents the carbon-fiber ply topology, but does leave a hollow cavity at the base of the stringer; in the actual specimen,

this region is filled with resin. Unfortunately, it is not possible to model this resin-rich region with shell elements (while the other benefits of using shell elements vastly outweigh this problem). However, the resin-filled region will be notably weaker than the other resin-carbon regions of the specimen, a relationship that is mimicked by having this hollow-region in the model. Additionally, this region is so small that the difference between having a resin-filled versus hollow region should not have a significant effect.

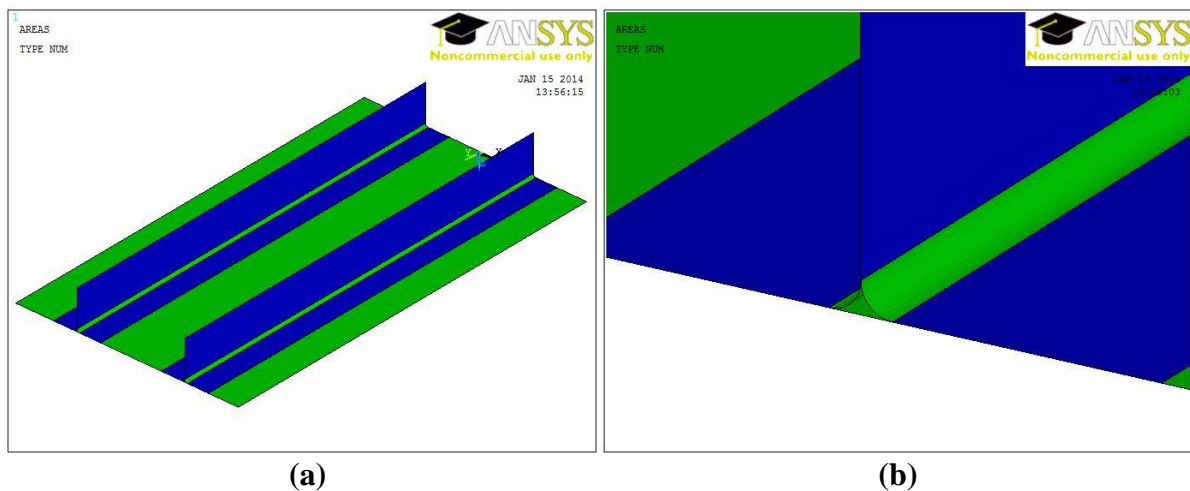


Figure 3.2: (a) Area thicknesses; (b) detail view of stringer base.

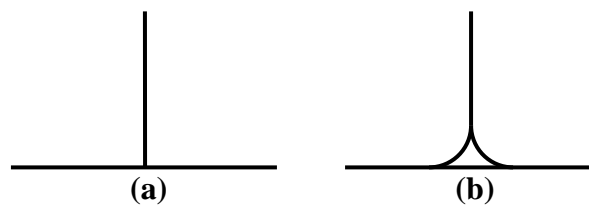


Figure 3.3: Stringer-plate interface options: (a) one and (b) two.

The orientation of individual layers follows the planned stacking sequence for the specimen. An 8 layer section is shown in Figure 3.4. The thickness of the layers was determined based on the dimensions of the actual specimen. Different areas of the specimen were measured using a micrometer, and then divided by the appropriate number of layers for that area. The thicknesses across the specimen were found to be non-uniform; areas with the identical number of layers were found to vary by as much as 0.178 mm. Additionally, the 16 layer sections were not found to be exactly twice as thick as 8 layer sections in all areas. In order to simplify the model development, average thickness values assuming that 16 layer sections were twice as thick as 8 layer sections were used. Under these assumptions, the 8 layer sections were modeled as being 1.194 mm thick, while the 16 layer sections were modeled as being 2.388 mm thick. Both numbers yield an individual layer thickness of 0.14925 mm.

Figure 3.5 shows various images of the completed model with all shell elements applied. Note that the displayed mesh size was not utilized in the modal analysis. Figure 3.5 depicts a global mesh size of 6.35 mm, while for model simulations a refined mesh was used. ANSYS will not process plotting thickness representations of multilayer shells with extremely fine meshes (due to computational demands), so a less refined mesh was used merely for displaying thicknesses in Figure 3.5. The final, finely meshed model used for testing consisted of 15,525 elements and is shown in Figure 3.6.

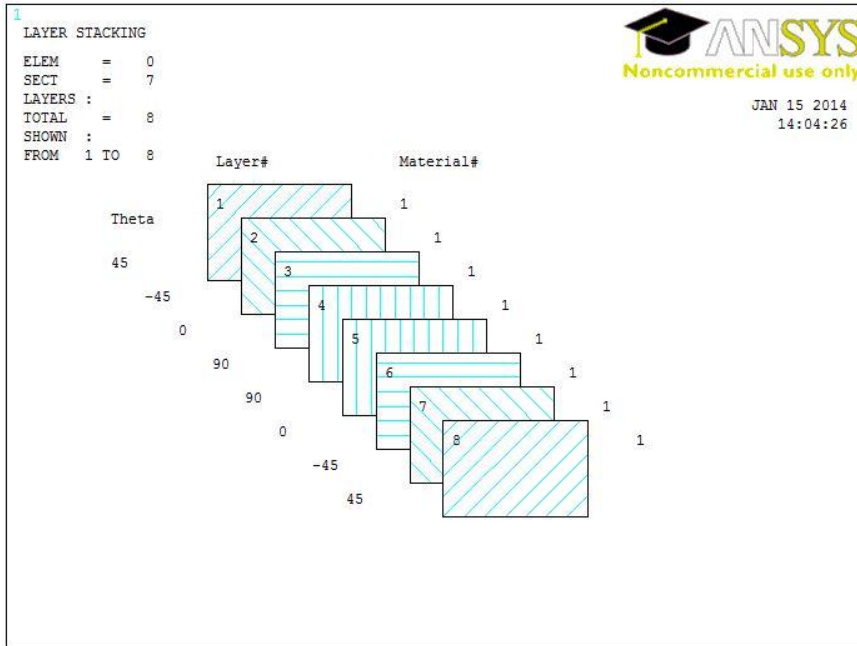
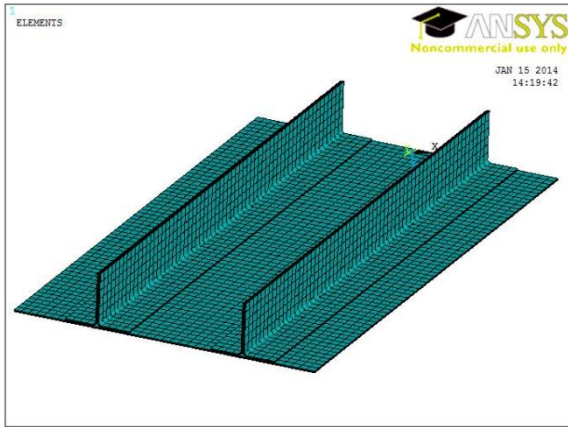
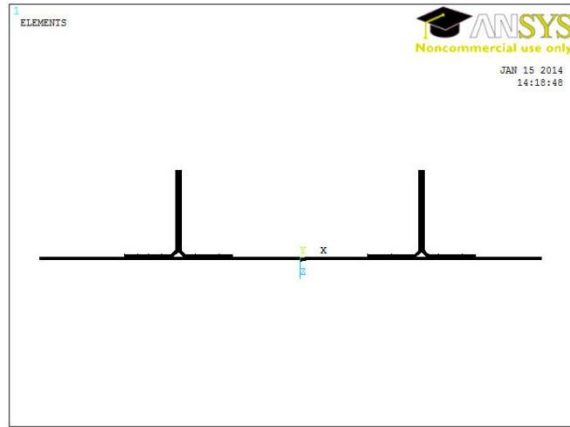


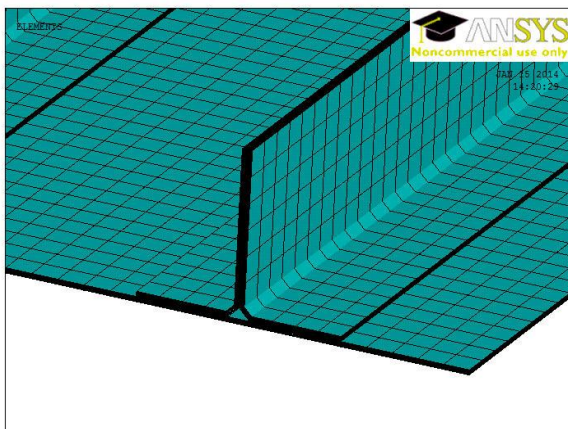
Figure 3.4: 8 Layer stacking sequence for the numerical model.



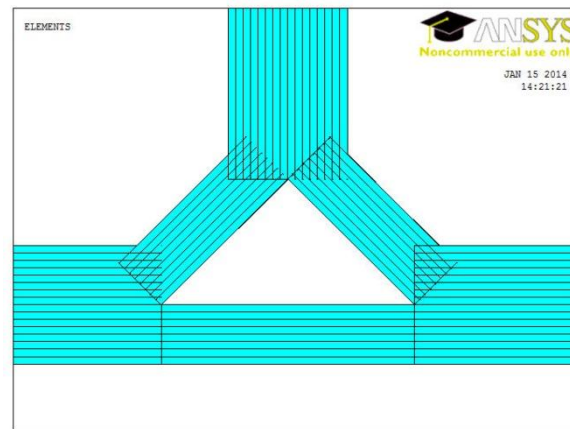
(a)



(b)



(c)



(d)

Figure 3.5: (a) Complete model display; (b) end-view of model; (c) stringer hollow-cavity detail; and (d) detail view of element layers.

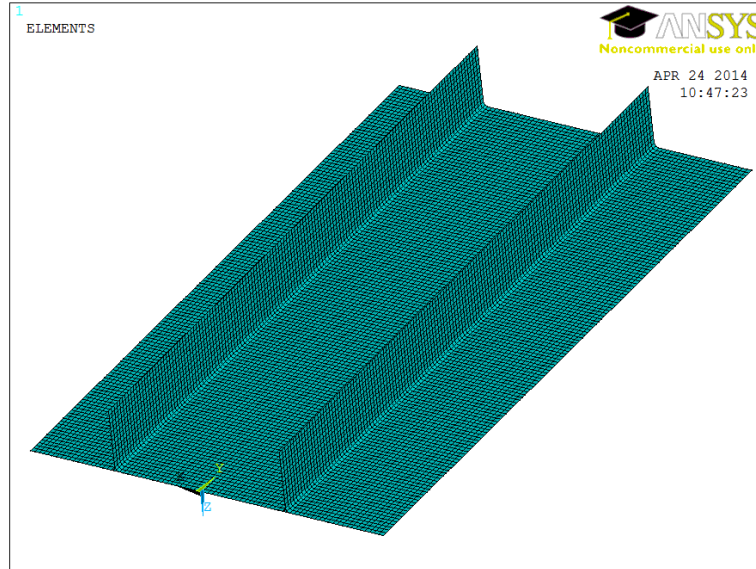


Figure 3.6: Final ANSYS model.

3.2 NUMERICAL MODEL PROPERTIES

Material properties for an individual layer of unidirectional carbon-epoxy composite were determined by a combination of experimentation and referencing of similar materials.

Table 1 displays the material properties used in the model.

Table 1: Model material properties.

Symbol	Description	Value
E_1	Young's Modulus in Fiber Direction	15.24 GPa
E_2	Young's Modulus 90° to Fiber Direction	3.10 GPa
E_3	Young's Modulus Out of Plane	3.10 GPa
ν_{12}	Major Poisson Ratio	0.3
ν_{21}	Minor Poisson Ratio	0.061
G_{12}	In-Plane Shear Modulus	6.21 GPa
G_{23}	Out-of-Plane Shear Modulus 1	6.21 GPa
G_{13}	Out-of-Plane Shear Modulus 2	6.21 GPa
ρ	Mass Density	1.60 g/cm ³

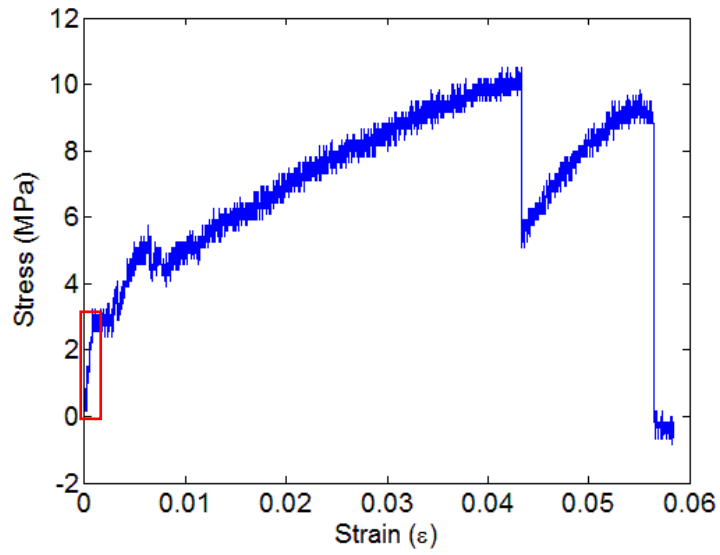
The two Young's modulus E_1 and E_2 were determined experimentally through tensile testing of representative coupons. Two each of four-layer 0° and 90° samples were prepared following the same VARTM process as for the stiffened panel. The specimen dimensions are given in Table 2.

The test was performed using an Instron universal tensile testing machine with an elongation rate of 2.54 mm/min. Strain calculations were performed based on crosshead displacement; although this is less accurate than mounting a strain gauge to the specimen, the goal of this experiment is to estimate material properties, so this was considered to be sufficient. Resulting head displacements are found in Table 2.

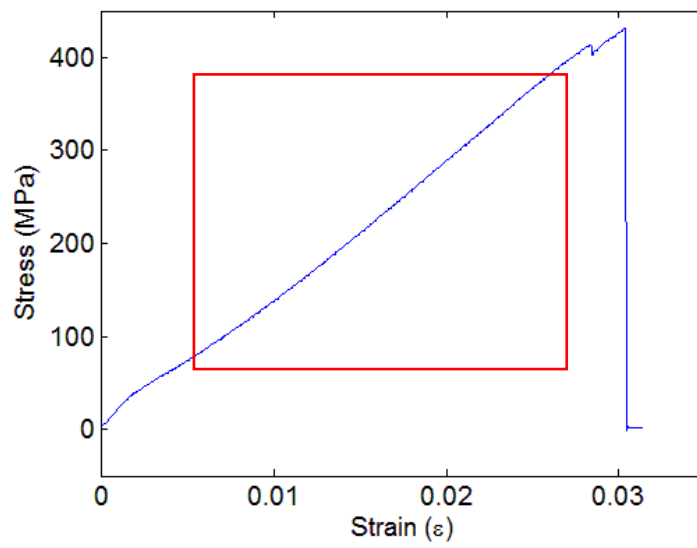
Table 2: Tensile testing coupon specifications.

Specimen Number	Unidirectional Fiber Orientation	Thickness	Width	Initial Distance Between Crossheads	Crosshead Displacement at First Break
1	90°	0.914 mm	28.70 mm	16.401 cm	7.188 mm
2	90°	0.914 mm	29.46 mm	17.099 cm	3.531 mm
3	0°	0.914 mm	27.96 mm	15.799 cm	4.420 mm
4	0°	0.914 mm	30.48 mm	16.800 cm	5.537 mm

The stress vs. strain plots obtained for specimens 1 (90° orientation) and 4 (0° orientation) are shown in Figure 3.7. Note that the plot for specimen 1 continues well past the elastic region of the carbon fiber. This happens because the dry fibers are held together by thin plastic stitching that runs perpendicular to the fiber direction. When the fiber fails after being loaded in the transverse direction, this plastic stitching picks up the loading until it too fails. Table 3 shows the resulting modulus estimations for each specimen based on the slope of the elastic region of the stress vs. strain curve for each specimen.



(a)



(b)

Figure 3.7: Stress vs. Strain for (a) specimen 1; and (b) specimen 4. Elastic regions boxed in red.

Table 3: Modulus estimations based on slope of elastic region of stress vs. strain curves.

Specimen	Property Estimated	Modulus Estimation
1	E_2	3.27 GPa
2	E_2	2.98 GPa
3	E_1	15.55 GPa
4	E_1	14.98 GPa

The resulting Young's modulus estimations are consistent with expected results; the modulus in the fiber direction is significantly greater than that in the transverse direction. Additionally, the pairs of samples testing the same fiber orientation had reasonably close estimations for Young's modulus. The resulting E_1 and E_2 values used for the model (as noted in Table 1) are the averaged results for the two samples in each test. Assuming that an individual layer of unidirectional carbon-epoxy composite is transversely isotropic, it is given that $E_3=E_2$.

The major Poisson ratio, ν_{12} , and mass density, ρ , are based on reference materials. Specifically, *Engineering Mechanics of Composite Materials* [10] and the product specification tables from ACP Composites [11] were used. In both cases, all unidirectional carbon-epoxy composites were found to have similar values for the major Poisson ratio and mass density. The minor Poisson Ratio, ν_{21} , was calculated based on the assumption that for orthotropic materials,

$$\nu_{21} = \frac{E_2}{E_1} \nu_{12} = \frac{3.10 \text{ GPa}}{15.24 \text{ GPa}} * 0.3 = 0.061$$

Lastly, the shear modulus values were found through fitting of the natural frequency measurement testing of the specimen, as the natural frequency values were dependent on the shear modulus values. This will be discussed in the following section.

CHAPTER 4 – EXPERIMENTAL TESTING

4.1 NATURAL FREQUENCY TESTING

There are two reasons for fitting the model to the specimen's natural frequency values. First, as noted above, this method will be used to identify the appropriate shear modulus values for the specimen. Secondly, if good correlation can be found between the specimen and model's natural frequencies values, then there is sufficient evidence to suggest the model is a good representation of the actual specimen.

The stiffened panel specimen was mounted to a vibration table such that it could be actuated at specified frequencies. The mounting system is shown in Figure 4.1.

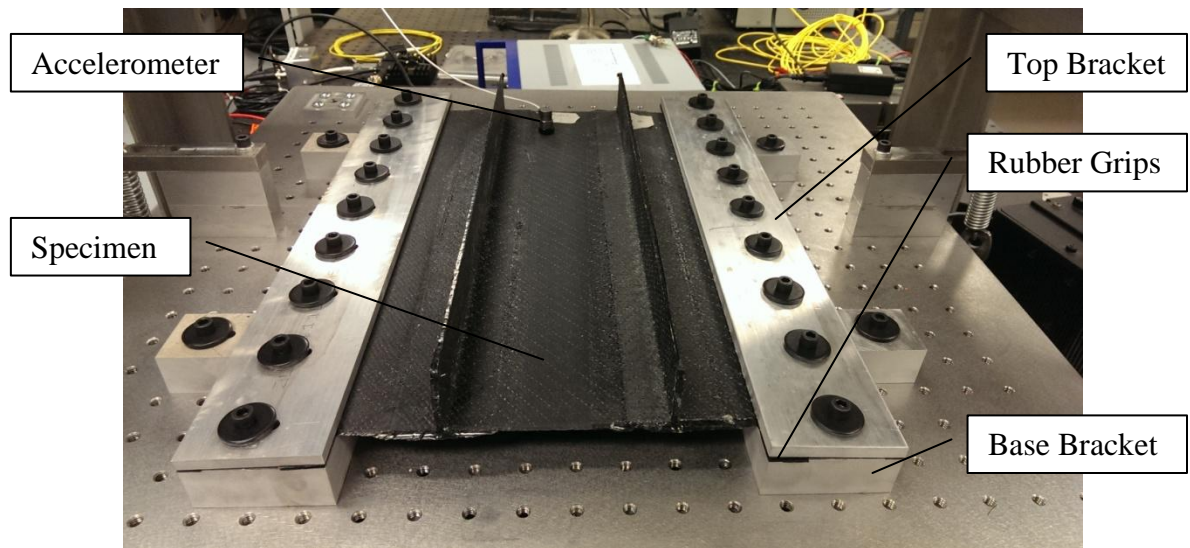


Figure 4.1: Stiffened panel specimen mounted on vibration platform.

The mounting system for the specimen consists of a set of aluminum base brackets rigidly bolted to a 2.54 cm x 2.54 cm grid stainless steel breadboard. The specimen sat on top of these base brackets and was clamped down by a pair of aluminum top brackets; these brackets are bolted down through the base brackets into the breadboard. Rubber sheets were placed on either side of the specimen surface to better distribute the load on the specimen and prevent local failure of the specimen edges. Although this rubber added some damping to the system, the rubber was sufficiently thin (0.79 mm) such that the specimen edges were still considered to be clamped.

In order to verify that the brackets are sufficiently rigid relative to the specimen, the relative in-plane rigidity of the specimen and mounting system were compared, with the rigidity being defined as

$$K = E * h * L \quad (2)$$

where E is the modulus of the material, h is the height of the material, and L is the length of the support mount. The relative rigidity calculated using equation (2) was found to be

$$\frac{K_{aluminum}}{K_{carbon/epoxy}} = \frac{(68.9 \text{ GPa}) * (25.4 \text{ mm}) * L}{(15.2 \text{ GPa}) * (1.19 \text{ mm}) * L} = 96$$

using E_1 for the composite panel. With aluminum being 96 times stiffer than the carbon, the boundary condition was assumed to be clamped in the finite element model of the specimen.

The vibration table consisted of a stainless steel 61 cm x 61 cm x 6.1 cm breadboard with a honeycomb core (ThorLabs PBH11105) mounted on a single-axis pillow-block assembly, as shown in Figure 4.2. The breadboard was actuated by a peizo-electric (PZT) stack actuator (PI P-840.40) mounted beneath the platform. Two adjustable turnbuckle-spring

biases were mounted on each side of the platform to constrain the motion of the board to small displacements. A low-voltage PZT amplifier provided a 50 V DC offset voltage to the PZT stack. The PZT stack was driven by a function generator, and at full power, had a stroke range of 60 microns +/- 20% and push force of 1000 N.

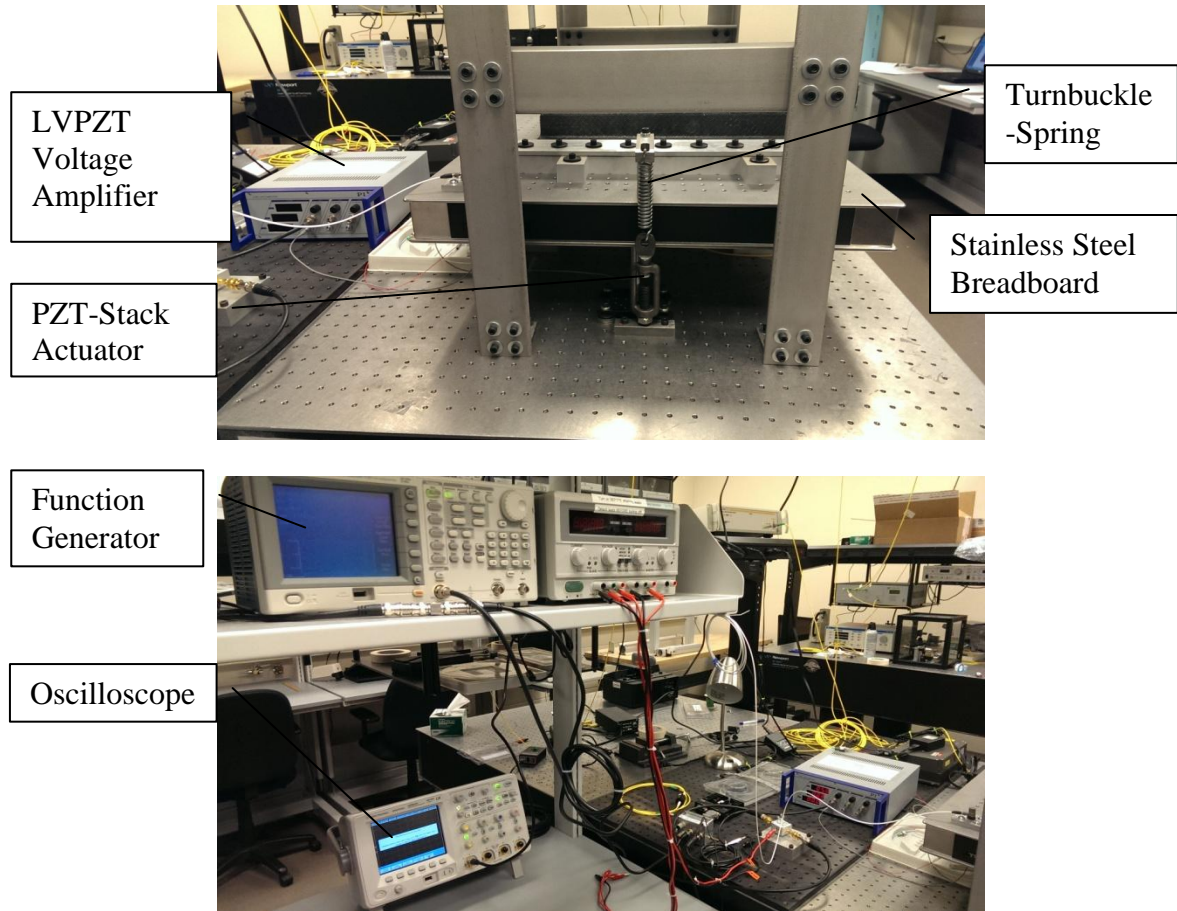


Figure 4.2: Vibration table components.

The accelerometer used to characterize the vibration table frequency components had a sensitivity of 100 mV/g (PCB Piezotronics C33). The accelerometer selected has an

operating range of 10-10,000 Hz, but was used up to 500 Hz in this experiment. It was mounted to the specimen using hot glue, with slight clamping pressure being applied while the glue set. This mounting method followed the manufacturer's guidelines, with the only detriment being a reduction in the high frequency range. As the sensor was only used up to a 500 Hz maximum frequency, this was not a concern for this test. The accelerometer was mounted in three different locations for this testing, with each location being subjected to the same frequency sweeps. This was done to account for the different mode shapes that will be present; one mode shape/natural frequency may be excited at one location but not another. These locations are shown in Figure 4.3. Note that the star is used as a location reference to Figure 4.1, where the star is drawn on the tape in the upper right corner of the specimen.

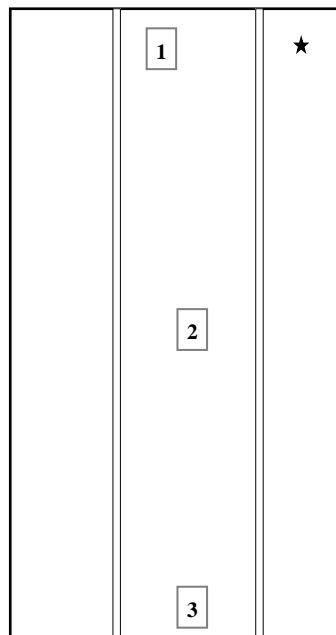


Figure 4.3: Accelerometer Mounting Locations

A sample of the data acquired with a driving frequency of 100 Hz at 6 V_{pp} and the accelerometer in position 1 is shown in Figure 4.4. A Fast Fourier Transform (FFT) was then applied to view the accelerometer data in the frequency domain. A plot of this same data after the FFT is performed is shown in Figure 4.5. Note that even though the driving frequency was 100 Hz, the oscilloscope measured the voltage response up to 1000 Hz to satisfy the Nyquist rule, which stipulates that the response must be measured up to at least twice the frequency of interest. Because the experiment will explore driving frequencies up to 500 Hz, it is necessary to sweep all driving frequencies up to 1000 Hz. In order to create a frequency response curve for the specimen, the driving frequency was swept from 30 Hz to 500 Hz at 5 Hz steps and 6 V_{pp}, with the peak amplitudes at each driving frequency being recorded. For the data shown in Figure 4.5, the peak amplitude was approximately 0.063 at 100 Hz. Collating these peak values and driving frequencies into a single plot yields an approximate frequency response curve for the specimen. This curve can then be used to identify which driving frequencies yield peak frequency response amplitudes, i.e. the natural frequencies of the specimen.

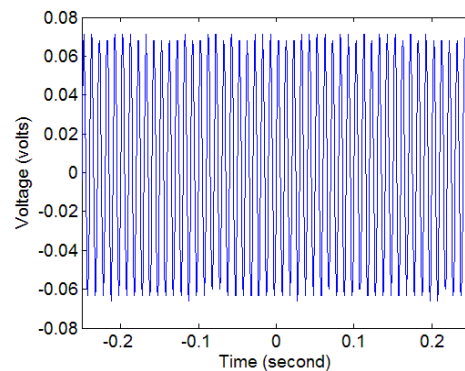


Figure 4.4: Voltage vs. time data at 100 Hz and accelerometer location 1.

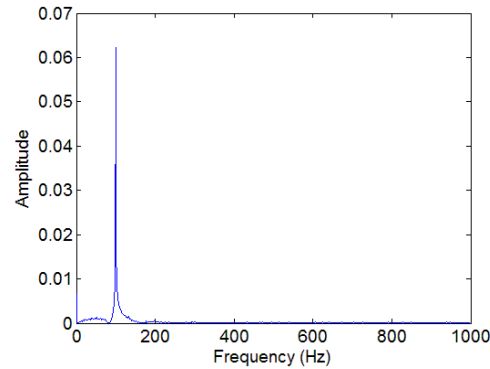


Figure 4.5: Frequency response at 100 Hz and accelerometer location 1.

A 5 Hz step size gave sufficient resolution to identify the approximate location of peaks in the frequency response. This means all natural frequencies are accurate within +/- 2.5 Hz. This was done due to limitations on data collection of the oscilloscope and to avoid violating the Nyquist rule. In order to increase precision of the measurements (thus allowing smaller step sizes for driving frequencies), it would be necessary to lower the oscilloscope's sweeping range from the previously discussed 0-1000 Hz range. Doing so would mean that the higher driving frequencies would violate the Nyquist rule requiring the frequency response of interest be swept to at least twice its value. With the next smallest oscilloscope sweeping range being 0-500 Hz, this would limit the driving frequencies to be investigated to a maximum value of 250 Hz. Because this test was aimed at driving frequencies from 30 Hz to 500 Hz, this was not an acceptable course of action. It was determined that a precision of +/- 2.5 Hz would be sufficient because the goal of this experiment is to verify that the FEA model produces similar results, not to identify the natural frequencies at high precision. Additionally, it should be noted that driving frequencies less than 250 Hz could take

advantage of the increased precision of the oscilloscope without violating the Nyquist rule. With this in mind, apparent natural frequencies less than 250 Hz were swept with this increased precision and found within a step size of 1 Hz, while apparent natural frequencies over 250 Hz maintain the 5 Hz step size and a ± 2.5 Hz accuracy.

The driving frequency values and associated amplitude values were recorded and then plotted together to produce the frequency response curves of interest. Before testing the specimen, the frequency response of the table itself was measured. For testing, the complete bracketing system, including all brackets and bolts, were included on the table; the only item not included was the specimen itself. This test was performed so that any resonances due to the table could be considered part of the driving force and not attributed to the specimen if they showed up in its response. For this initial test, the accelerometer was mounted directly to one of the breadboard screw slots.

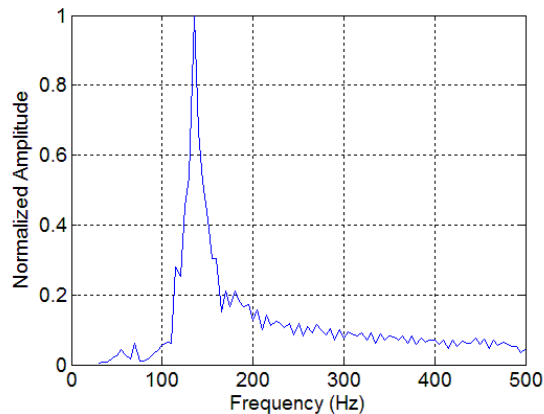


Figure 4.6: Frequency response curve for vibration table and mounting system.

The resulting frequency response curve for the table and mounting frame is given in Figure 4.6. The frequency response curve for the table and brackets shows a clear peak at 134 Hz. The response at higher frequencies displays an oscillation pattern that yields no distinct peak amplitudes.

Following the table measurement, the complete sweep from 30 Hz to 500 Hz was performed on the specimen for each accelerometer location shown in Figure 4.3. Figure 4.7 displays the frequency response curves for the specimen obtained with the accelerometer at the three different locations. In each of the cases shown in Figure 4.7, any peak amplitudes seen at 134 Hz can be attributed to the table/bracket vibration and will be ignored. With that in mind, the remaining peaks in the frequency response curves should be the natural frequencies of the specimen. Table 4 lists the natural frequencies from each accelerometer location and the cumulative list of natural frequencies identified for the specimen. Not all natural frequencies will necessarily be identified with only three accelerometer locations, however it is expected that most will be measured in at least one location. This list will be used as the experimental result for natural frequencies of the specimen. Note that the 56 Hz peak seen at location 2 and barely evident at location 3 is not as distinct as the other peaks noted in Table 4, but is believed to be a natural frequency and included in the list for model fitting reasons. This will be discussed in the Model Fit Analysis section.

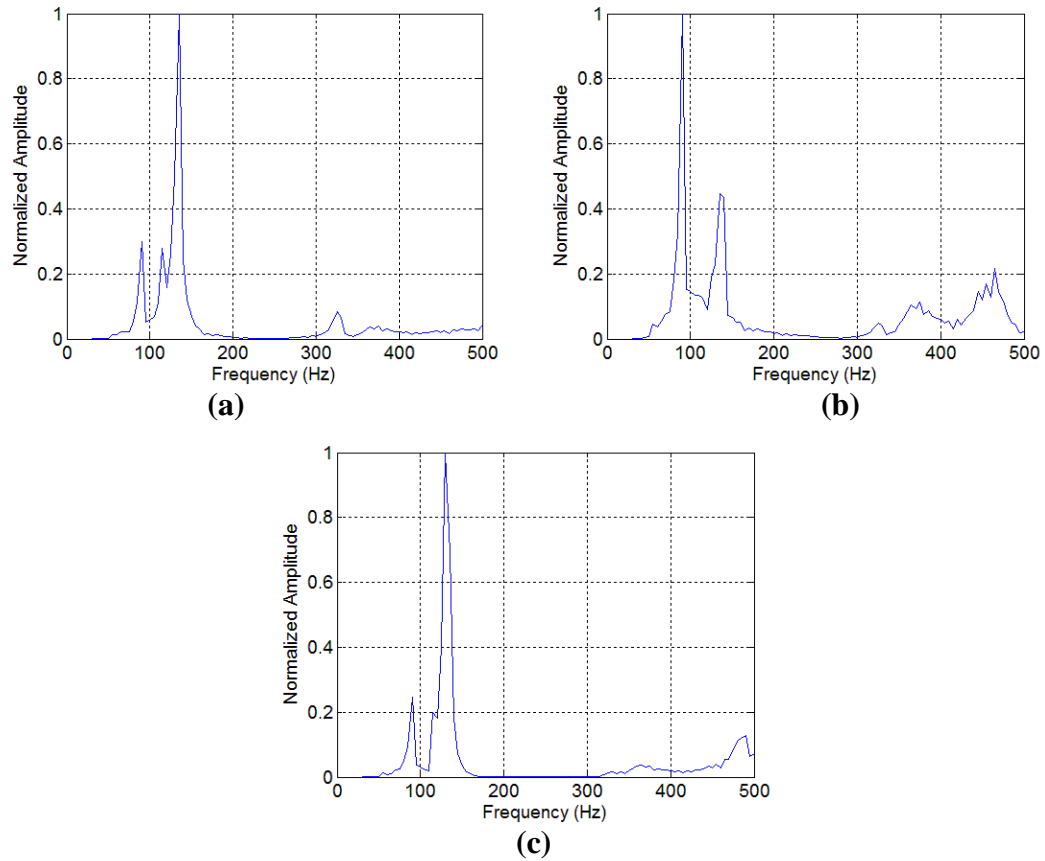


Figure 4.7: Frequency response curves for the specimen at accelerometer locations (a) one, (b) two, and (c) three (see Figure 4.3).

Table 4: Measured specimen natural frequencies. All values are in Hz.

Accelerometer Location			Cumulative Specimen Natural Frequencies
1	2	3	
	56	56	56
88	88	88	88
325	325		325
	365		365
	375		375
	445		445
	455		455
	465		465
		390	490

4.2 MODEL FITTING

The ANSYS model discussed in Chapter 3 can now be compared to the experimental results. For modal analysis, a final refined mesh consisting of 15,525 elements was used, based on the model convergence.

The specimen was clamped over a width of 11.9 mm on each side. To model this, nodes were constrained to have no displacement or rotation in all directions in this region, as shown in Figure 4.8. This replicates the same surface area to be constrained in the model as in the test specimen.

As noted in Section 3.2, the elastic modulus values were determined experimentally, while the Poisson ratio and density were identified based on known values for carbon-epoxy composite references. The shear modulus could not be determined in this manner because it varied significantly from one reference material to the next. Thus, with all other properties fixed, it was determined to select a starting value for the shear modulus based on a reference material and adjust this value to best fit the experimental results for natural frequencies. If a good match between the model natural frequencies and experimental results can be found while maintaining a realistic shear modulus (realistic meaning within the range of reference materials), it is reasonable to say that the selected shear modulus is fairly accurate. This method will simultaneously identify the proper shear modulus values of the material and verify the model's accuracy.

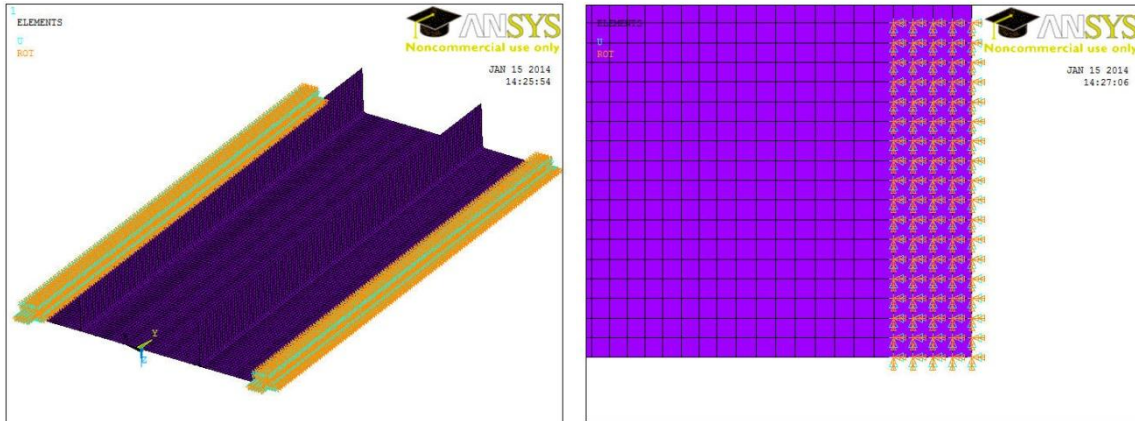


Figure 4.8: Model boundary conditions.

The initial modal calculations with the model were performed with the shear modulus of a known carbon/epoxy (IM6G/3501-6) material, $G_{12}=G_{23}=G_{13}=6.48$ GPa [10]. It is expected that $G_{12}=G_{13}$ (based on geometry) while G_{23} would have a different value. However, in the many iterations tested, it was found that changing G_{23} or G_{13} within a realistic range had very little effect on the resulting natural frequency values; the only noticeable changes occurred at very high frequencies and resulted in a change of only a few Hz to these modes. It was determined to set $G_{12}=G_{23}=G_{13}$ because any changes to G_{23} or G_{13} away from the value of G_{12} caused minimal changes to the natural frequency results. After many iterations of changing the shear modulus values and performing modal calculations in the model, the final values for the shear modulus were set at $G_{12}=G_{23}=G_{13}=6.21$ GPa, only a 4.3% difference from the initial value. Because of this small percent difference, this is a reasonable result. The resulting natural frequency values derived in the model are given in Table 5. Table 6 offers a side-by-side comparison of the results from the model and experiments.

Table 5: Natural frequencies calculated through finite element model.

Mode Number	Frequency (Hz)
1	60.6
2	85.9
3	184.5
4	194.2
5	354.7
6	376.7
7	396.7
8	435.3
9	450.3
10	462.2
11	479.8

Table 6: Comparison of natural frequency results. Mode numbers are taken from finite element model.

Mode Number	Model Natural Frequencies	Experimental Natural Frequencies
1	60.6	56
2	85.9	88
3	184.5	
4	194.2	
		325
5	354.7	365
6	376.7	375
7	396.7	
8	435.3	445
9	450.3	455
10	462.2	465
11	479.8	490

Overall, the model and experimental results compared well; 8 of the 11 natural frequencies less than 500 Hz found in the model had obvious correlating values in the experimental results. At this point, it is important to point out the known differences between

the finite element model and actual test specimen that would affect the natural frequencies predictions:

1. The boundary conditions in the model differed slightly from those of the experimental tests. The model assumes a uniformly constrained boundary, while the experimental version is mounted with 9 bolts along a clamp on each side. Although effort was made to spread the clamping pressure evenly by using a large number of bolts and to tighten the bolts uniformly, it is impossible to create a perfectly uniform boundary condition in this manner. In addition, any damping behavior of the rubber during the vibration loading in the experimental testing was not modeled.
2. The model represented a perfectly uniform specimen. Although the specimen was generally consistent in dimensions, areas with the same number of layers varied in thickness by as much as 0.178 mm.
3. The model included a hollow region beneath the stiffeners, while in the actual specimen this area was filled with resin.

These points account for the small frequency shifts between the predicted and experimentally measured natural frequencies. There are, however, three discrepancies that must be discussed in more detail. First, three natural frequencies were predicted in the model calculations (numbers 3, 4, and 7 at 184.5 Hz, 194.2 Hz, and 396.7 Hz) but not measured experimentally. The model can mathematically identify a mode excitation anywhere on the geometry; the experimental data, on the other hand, relies on the accelerometer's ability to read these excitations. If the accelerometer is not in a location that catches a significant displacement due to mode excitation, it will not register the frequency as being excited.

Although the accelerometer was moved around the specimen, it is perfectly reasonable to believe it would still not catch every excited mode. For example, Figure 4.9 shows the calculated mode shape of mode 7 (at 396.7 Hz). Even though the model was able to see this as a natural frequency, it was missed in the experimental trial, likely because the excitation of the mode had nearly no displacement effect on the accelerometer at any of its locations.

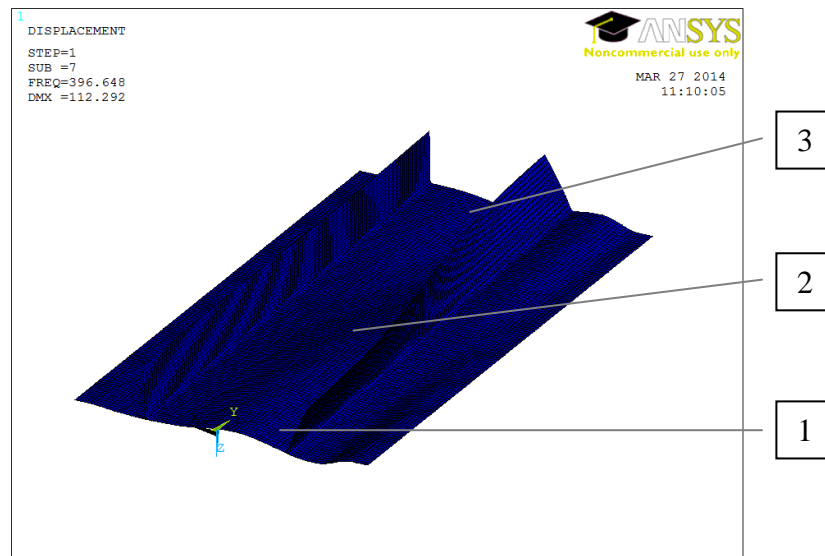


Figure 4.9: Calculated mode shape of mode 7 and accelerometer locations.

Secondly, the more difficult discrepancy is the 325 Hz frequency seen experimentally, but not seen in the model predictions. There are two potential explanations for this natural frequency:

1. The 365 Hz and 375 Hz peaks measured experimentally are fairly close together and could actually correspond to a single peak at 375 Hz (see Figure 4.7(b)), which would

correspond to the model peak at 376.7 Hz. This would leave the experimental mode seen at 325 Hz to correspond to the model peak at 354.7 Hz; the difference in these frequency values could be accounted for by the general sources of error discussed previously.

2. This is an artificial peak resulting from mounting the specimen to the table. Although the table was tested independently to account for its effects, there may be some other aspect introduced when clamping the specimen into place (i.e. introducing a new natural frequency due to vibrating bolts, washers, or the top bracket based on the altered geometry with the introduction of the specimen).

Although the exact origin of this one peak cannot be identified, the close matching of the other frequencies indicates that the model is a very good representation of the specimen. Thirdly, it was noted that the 56 Hz peak measured experimentally was not as distinct as the other peaks listed in Table 4. The reason it is still believed to be a natural frequency of the system is because without it, the first natural frequency would have to be at 88 Hz. In order to match this, the model would require that the shear modulus be set to $G_{12}=G_{23}=G_{13}=20.7$ GPa. This is significantly higher than the reference materials' values for the shear modulus, so is therefore considered unreasonable. By including the less-distinct peak at 56 Hz in the experimental results, the shear modulus for the model is able to stay at a reasonable value.

Overall, the model results are considered to be a good match to the experimental results. This confirms that the FEA model is a good representation of the actual specimen and will therefore be used for future predictions of the specimen response.

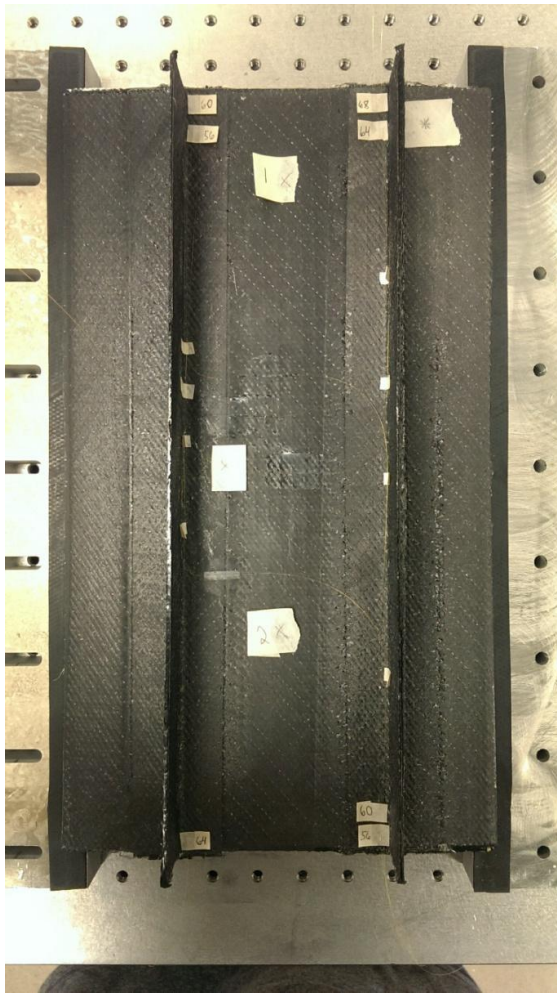
4.3 VIBRATION AND IMPACT DATA COLLECTION

The FBG sensors were surface mounted to the specimen using M-Bond 200 strain gauge glue. Surface mounting was selected in lieu of embedding the sensors due to the added complications of embedding sensors, as discussed previously. Before being mounted, the surface was prepared by smoothing with 60 grit sandpaper and cleaned with isopropyl alcohol. Figure 4.10 shows the mounted FBGs, while Figure 4.11 shows their specific locations. Note the masking tape in Figure 4.10 was used to hold the various fiber optic cables in place. In Figure 4.11, FBGs A and C fall directly on the transition from 16 layer to 8 layer thickness. The FBG sensor numbers correspond to the Bragg wavelengths shown in Table 7. The Nominal Bragg Wavelength is the value reported by MicronOptics, while the Measured Bragg Wavelength corresponds to the measured Bragg wavelength using a MicronOptics Spectrometer (siFBG-FS-700XP) after the sensors were mounted.

Damaged was introduced to the specimen through multiple impacts. After each impact, the dynamic response of the specimen was recorded using the mounted FBG sensors. The dynamic response was recorded for no vibration, and with the PZT actuator driven by a function generator at excitation frequencies of 88 Hz, 150 Hz, and 325 Hz. A peak-to-peak amplitude of 6 V was used in all cases. The 150 Hz driving frequency follows previous research [7] and simulates aircraft in-flight vibration, while the 88 Hz and 325 Hz values correspond to natural frequencies of the specimen.

Table 7: FBG sensor labels and corresponding Bragg wavelengths.

Sensor Label	Nominal Bragg Wavelength	Measured Bragg Wavelength
A	1556	1555.95
B	1560	1560.13
C	1564	1564.13
D	1568	1568.09



(a)



(b)

Figure 4.10: (a) Mounted FBG sensors on stiffened panel and (b) detailed view of sensors.

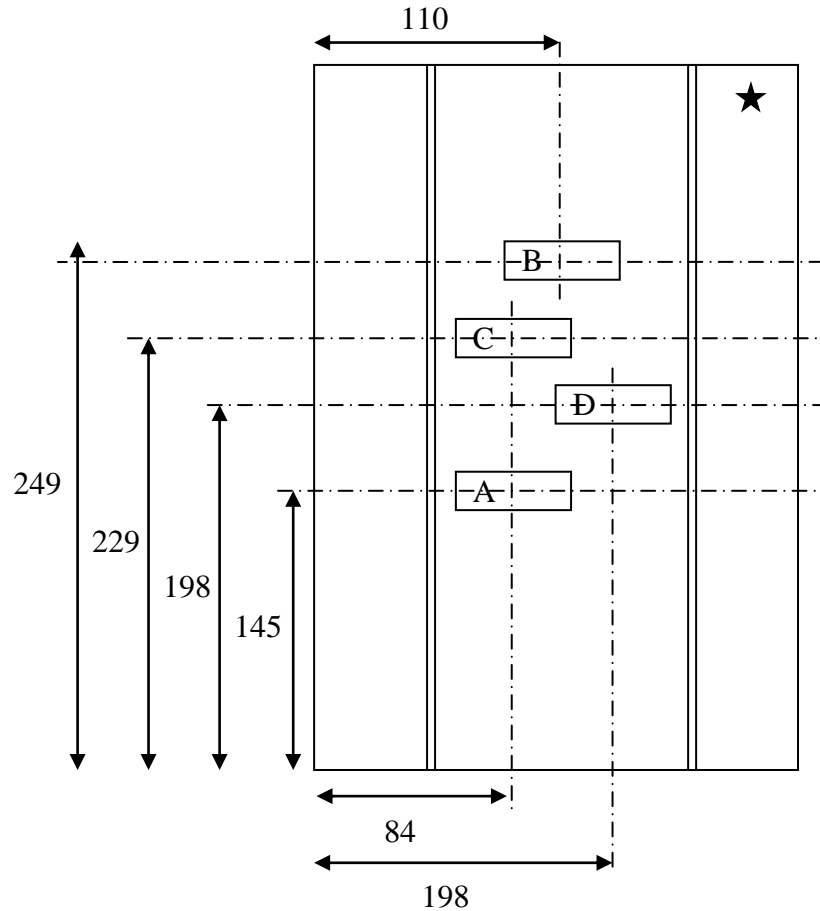


Figure 4.11: FBG locations. All dimensions in mm.

The process of collecting impact damage was as follows:

1. Measure dynamic response of undamaged specimen
2. Impact the specimen at location 1
3. Measure the dynamic response of the damaged specimen (one damage location)
4. Impact the specimen at location 2
5. Measure the dynamic response of the damaged specimen (two damage locations)
6. Impact the specimen at location 3

7. Measure the dynamic response of the damaged specimen (three damage locations)
8. Impact the specimen at location 4
9. Measure the dynamic response of the damaged specimen (four damage locations)

Impacts were performed using a PCB Piezotronics impact hammer (Model 086C02) with a round impact head approximately 5 mm in diameter. Initially, it was planned to use the impact hammer to record impact forces, but the hammer malfunctioned and did not record data properly, so this data was not utilized. All impacts were performed on the skin side of the panel, with the panel mounted as shown in Figure 4.12. Impact locations are shown in Figure 4.13, and detailed images of the impacts are shown in Figure 4.14. Note that Impact 1 seemed to produce a double impact, while Impact 2 clearly protruded completely through the specimen, causing minor splintering on the reverse side.

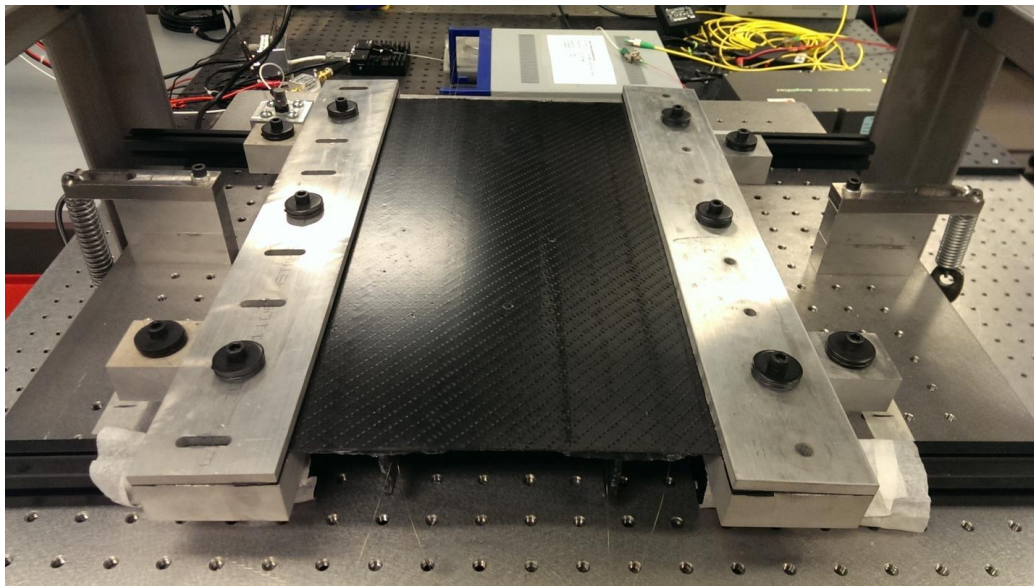


Figure 4.12: Stiffened panel mounted for impact testing.

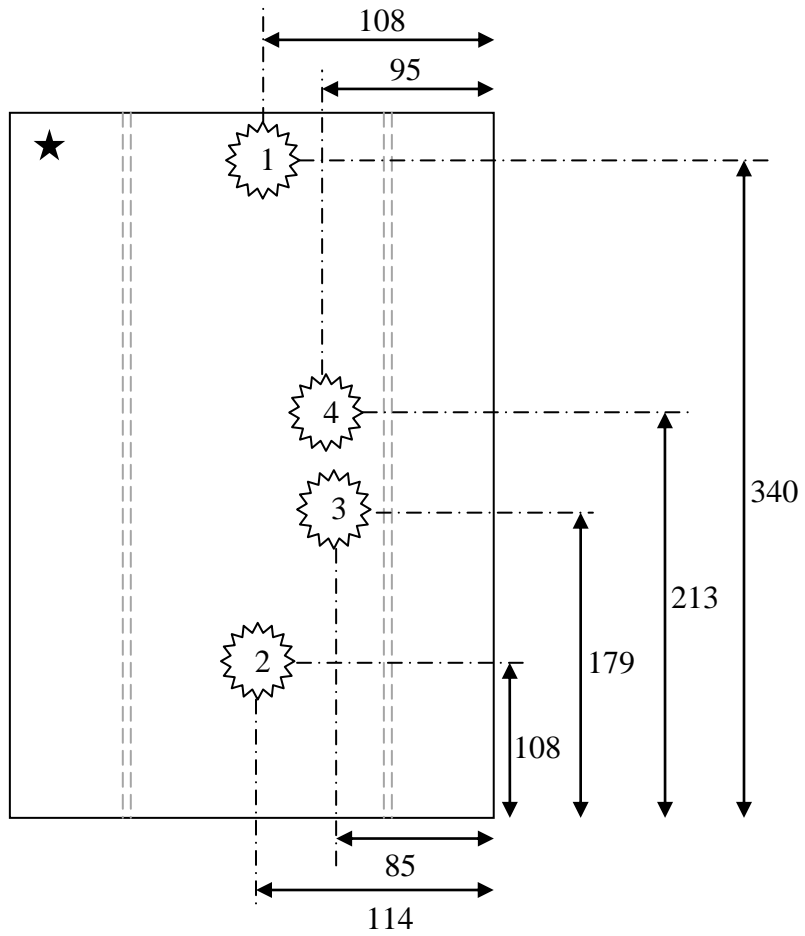
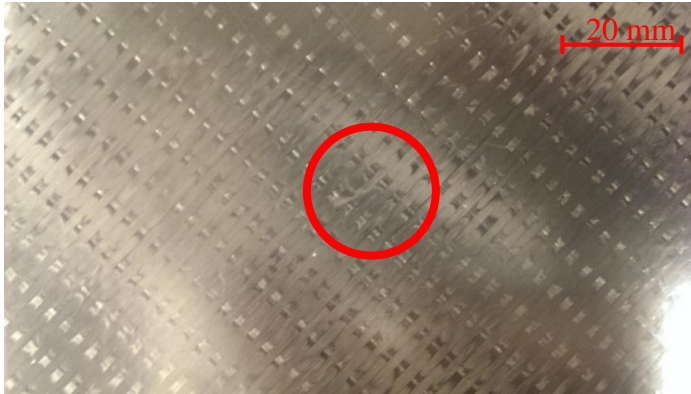


Figure 4.13: Impact locations, skin-side of panel. All dimensions in mm.

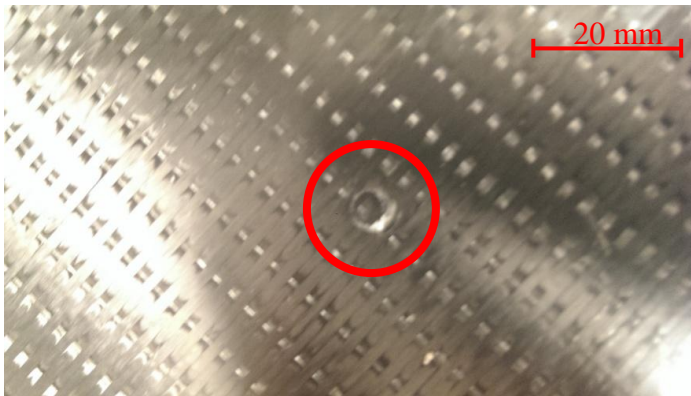
Figure 4.14: Detailed view of impacts: Impact 1 (a) skin side and (b) stiffener side; Impact 2 (c) skin side and (d) stiffener side; Impact 3 (e) skin side and (f) stiffener side; and Impact 4 (g) skin side and (h) stiffener side.



(a)



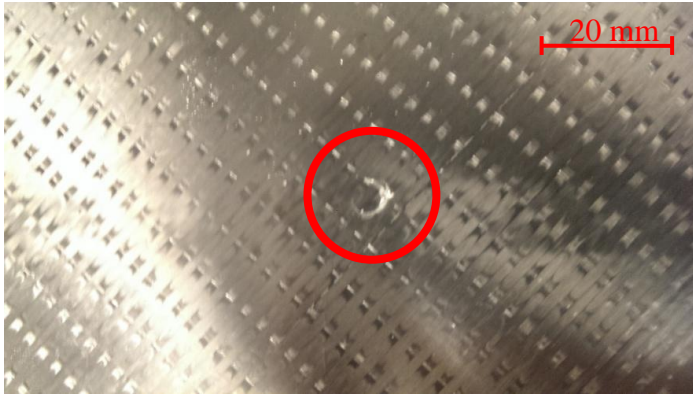
(b)



(c)



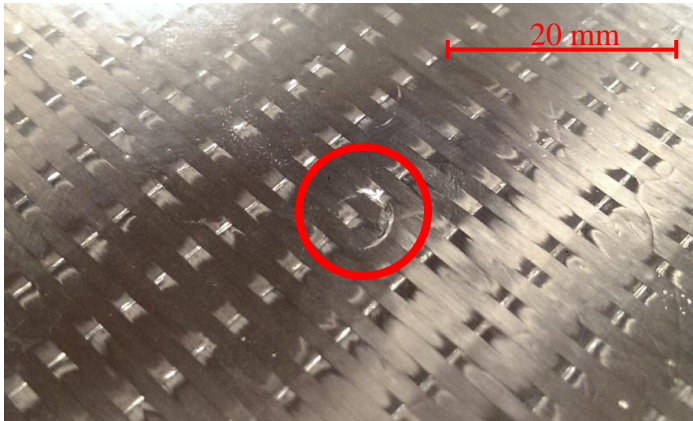
(d)



(e)



(f)



(g)

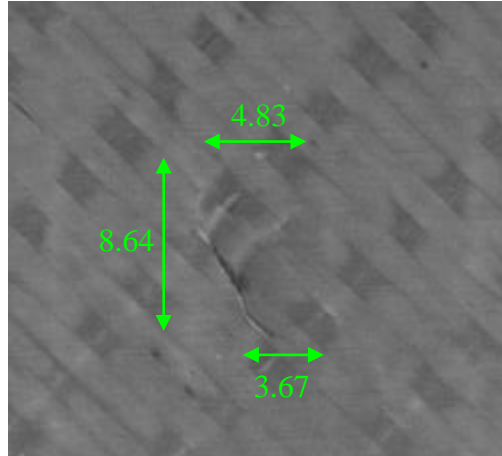


(h)

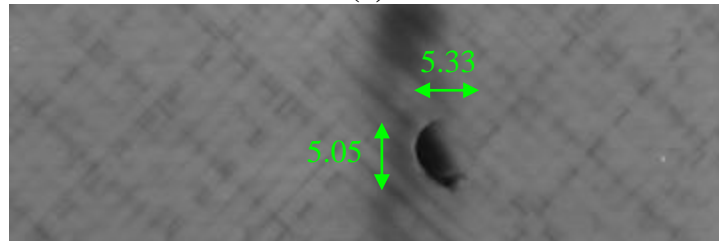
Micro-CT scans of the specimen were taken in order to identify the extent of the damage applied by each impact. According to the scans, impacts 1, 3, and 4 did not seem to propagate much beyond the basic shape of the impact head (circular). The CT scans for these impacts can be found in Figure 4.15. Impact 2 caused progressive damage that spread away from the impact location. Figure 4.16 shows the CT scans of the progressive damage found for Impact 2.

The full-spectral response in reflection of all FBG sensors subject to vibration in this study was acquired with a dynamic, full-spectral interrogator recently developed within the lab [5]. Full details of the interrogator and post-processing can be found in Vella *et al* [4]. Figure 4.17 shows a block diagram of the system, along with a picture of the physical components.

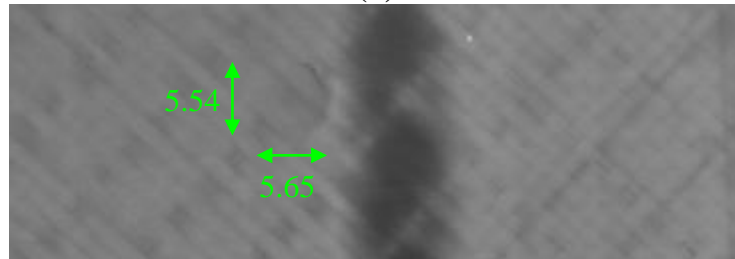
The amplified spontaneous emission (ASE) laser source provides a wide bandwidth lightwave signal that is then amplified by an erbium doped fiber amplifier (EDFA). This amplification increases the power going to the FBG, and in turn, the micro-electro-mechanical (MEMs) filter that records the reflected spectrum. The tunable MEMs filter is driven by a function generator, and powered by a DC power source. By adjusting the driving frequency, the MEMs filter can be set to sweep at different speeds and different wavelength windows. There is an inherent compromise between time resolution, wavelength window and wavelength resolution. For all tests in this study, the MEMs filter was set to sweep at 10 kHz as frequency components above 5 kHz were not expected.



(a)



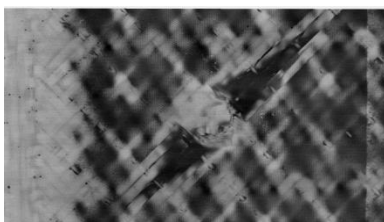
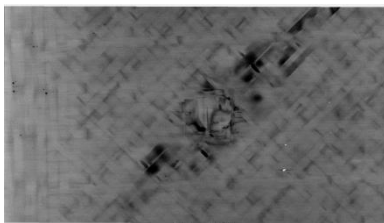
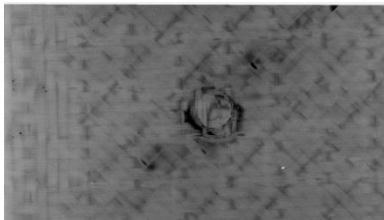
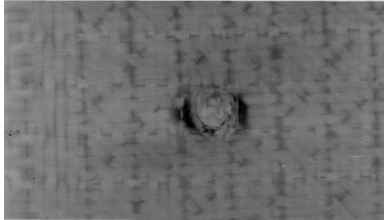
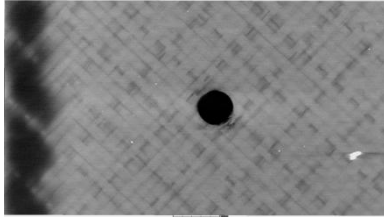
(b)



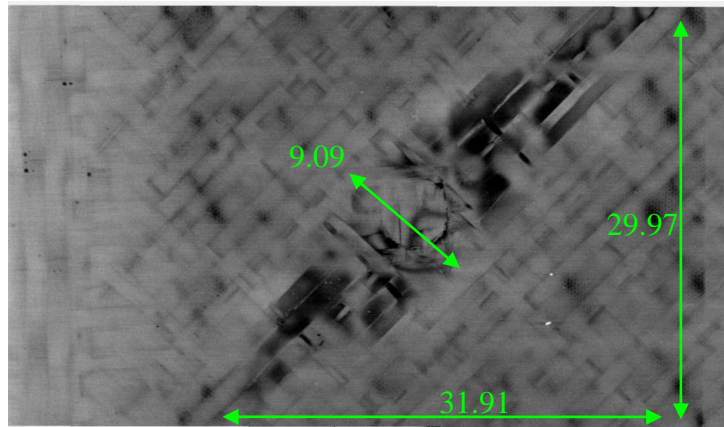
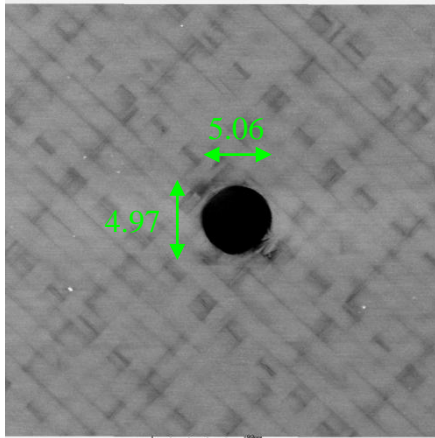
(c)

Figure 4.15: CT scan of impact locations (a) 1, (b) 3, and (c) 4. All dimensions in mm.

Figure 4.16: CT Scan of impact 2 (a) progressive damage and (b) detailed view of damage. All dimensions in mm.



(a)



(b)

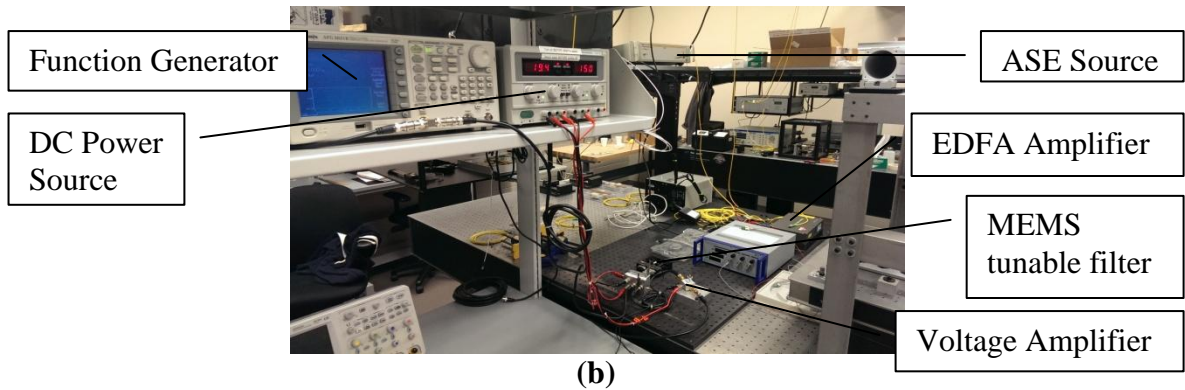
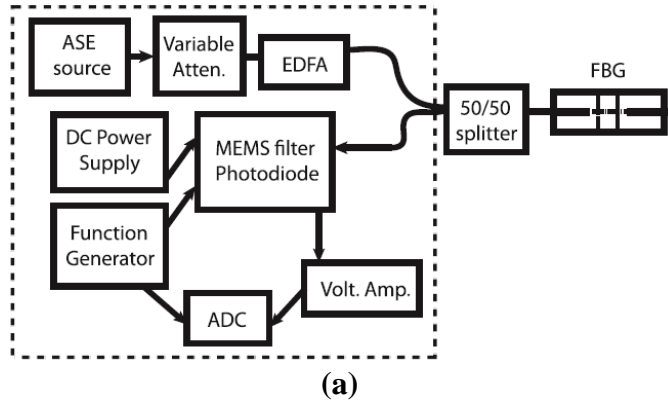


Figure 4.17: (a) Block diagram and (b) photograph of FBG full-spectral interrogator

Although the ASE source produces a wide bandwidth lightwave signal, the EDFA amplifies a limited range of this bandwidth. Together, the ASE and EDFA combination produces the non-uniform intensity spectrum shown in Figure 4.18. The result is a non-uniform intensity distribution across each of the FBG sensors, as measured in Figure 4.19(a). This effect causes the time response of the FBG sensors to appear at different intensities, as shown in Figure 4.19(b). This difference in intensity for the different sensors is not detrimental to this study because peak shifts are being measured; as long as individual peaks can be discerned, their relative intensity is of little importance.

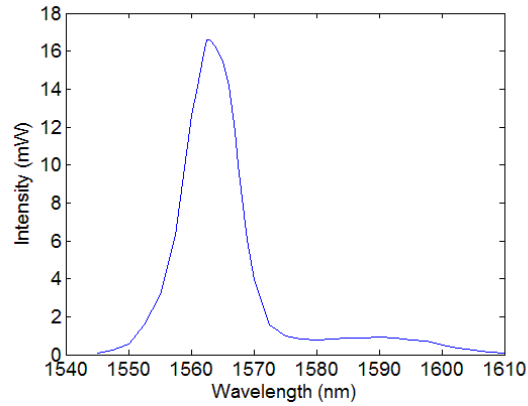


Figure 4.18: ASE-EDFA output intensity spectrum.

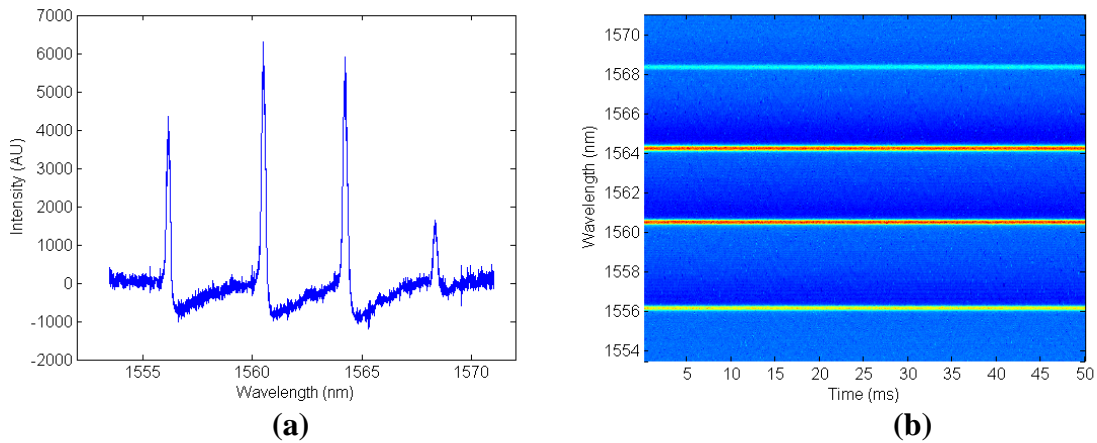


Figure 4.19: (a) Reflection spectrum and (b) time response of mounted FBG sensors on the undamaged, non-vibrating specimen. In (b), the colorscale corresponds to reflected intensity with red as maximum intensity.

In addition to recording post-impact vibration data, the FBGs were also interrogated during the impacts in order to record the response to an impact event. These interrogations were performed at 10 kHz, with a sample acquisition rate of 50 Msamples/sec. Although this data is not utilized in this study, it is still potentially informative and was recorded for future

use. Figure 4.20 shows the FBG responses to the impact events. It represents the first time that the full-spectral response of multiplexed sensors have been measured at a dynamic rate ($> 1\text{kHz}$).

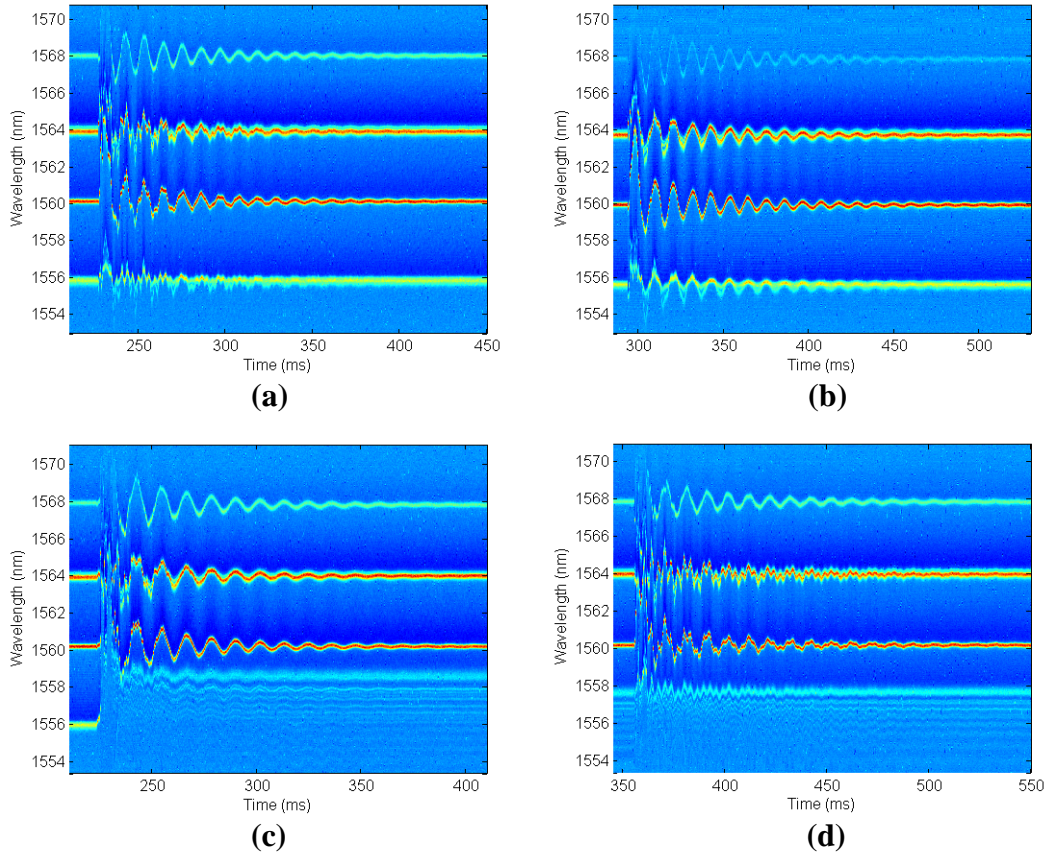


Figure 4.20: Wavelength spectrums for impacts (a) one, (b) two, (c) three, and (d) four.

Figure 4.20(c) shows clearly that FBG A was broken during impact three. Before the impact, there is a clear single peak, but after the impact, there is a significant number of interference fringes across a wide bandwidth. This measurement is indicative of a fracture in the FBG. As the measurement is in reflection, the portion before the fracture could still be

measured. However, the relation of the deformation of this sensor to that of the stiffened panel is not known and any data from FBG A after impact 3 should not be utilized.

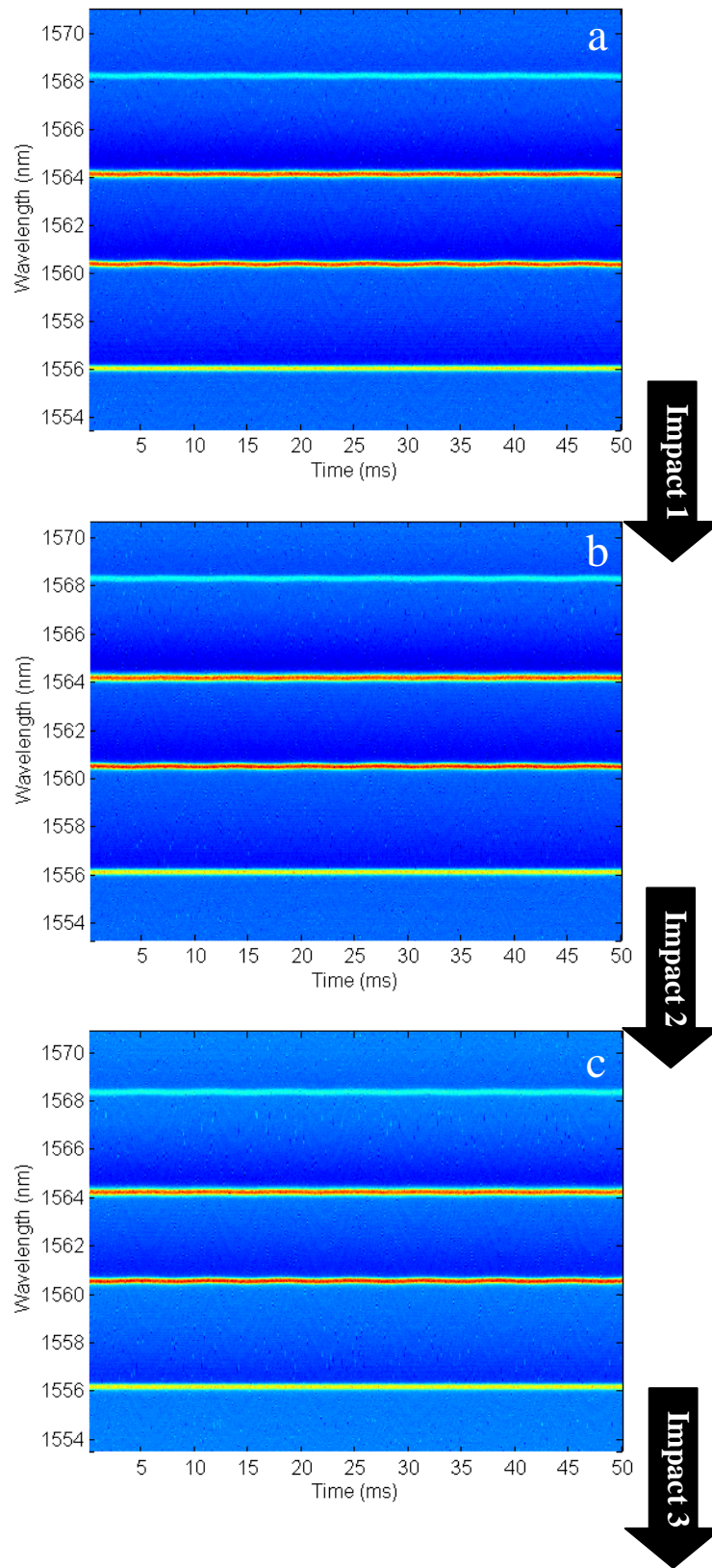
4.4 VIBRATION AND IMPACT TEST RESULTS

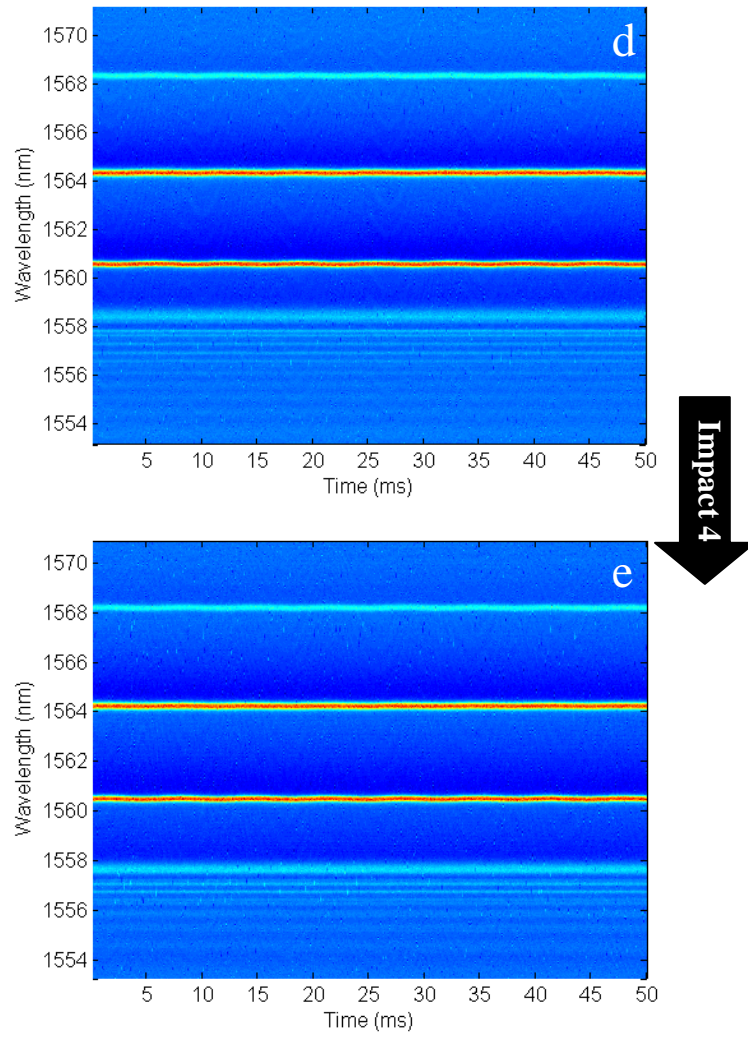
As outlined in detail previously, the FBGs were interrogated while the specimen was subjected to harmonic vibration. This harmonic vibration was driven by the PZT stack, which was governed by the function generator producing 88 Hz, 150 Hz, and 325 Hz signals. Each driving frequency was interrogated independently. This thesis will focus on the results of the 150 Hz vibration testing as it is the most relevant to in-flight measurements of an aircraft. These interrogations were performed at 10 kHz, with a sample acquisition rate of 100 Msamples/sec. This high sample acquisition rate was necessary in order to collect enough samples to produce reliable Fourier Transform results in later calculations.

Figure 4.21 displays the dynamic response for each post-impact case when the stiffened panel was subjected to vibration at a driving frequency of 150 Hz. All sensors were measured simultaneously, through a full sweep of the entire wavelength window. Due to the large wavelength window presented, it is difficult to see the changing time response of each sensor.

When comparing Figures 4.19(b) and 4.21(a), it is clear that the strain in the specimen is being effectively transferred to the FBG sensors by the strain gauge glue; Figure 4.19(b) shows constant peak locations, while Figure 4.21(a) shows a slight oscillatory pattern to the peak, corresponding to the 150 Hz vibration. The change in FBG A response from Figure 4.21(c) to Figure 4.21(d) is consistent with the fractured FBG response seen during the impact event.

Figure 4.21: Dynamic response of FBG sensors to 150 Hz excitation: (a) undamaged, (b) post-impact 1, (c) post-impact 2, (d) post-impact 3, and (e) post-impact 4.





Outside of these general conclusions, there is not much information to be garnered from these plots; more interesting information can be found by converting this data to the frequency domain.

To convert the raw full-spectral data sets shown in Figure 4.21 to the frequency domain, the peak wavelength location over time of each FBG was extracted. These values were then normalized to zero by subtracting the average Bragg peak location of each FBG over time. This yields a relative wavelength shift for each FBG. This wavelength shift information can be converted to strain using equation (1). In this case, the initial wavelength will be the initial value after surface mounting because pre-mounting data was not recorded, and p_e is known to be ~ 0.22 for silica [12]. Using equation (1), the relative wavelength shift data can be converted to strain information as shown in Figure 4.22.

The fast Fourier transform (FFT) was computed to view the averaged frequency components that exist within the dynamic signal, as shown in Figure 4.23. As expected, the primary driving frequency for the FBGs on the undamaged specimen was seen at 150 Hz. It is worth noting that although FBG A does show a slight peak at 150 Hz, it is barely above the noise level. When the specimen was tested at an excitation frequency of 325 Hz, FBG A did show a distinct peak at 325 Hz, while FBG D fell into the noise region. These results were consistent with the mode shapes based on the accelerometer responses discussed previously.

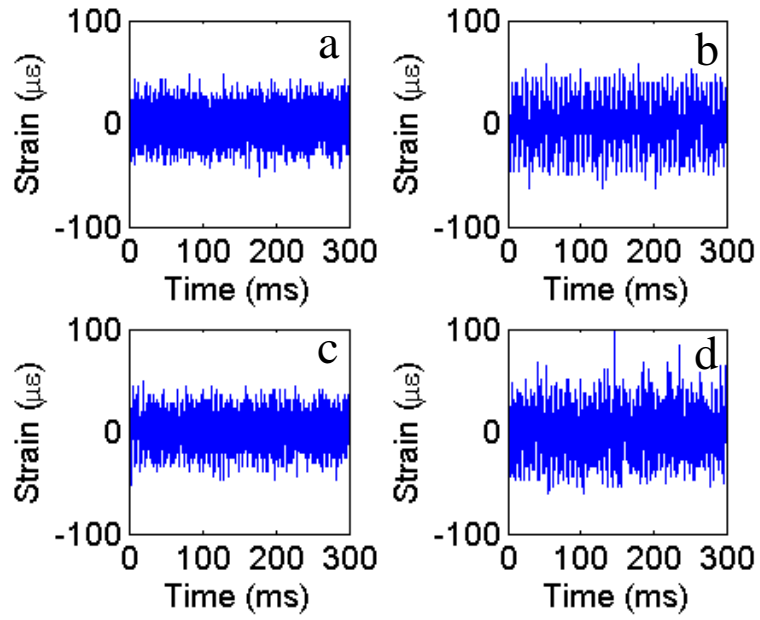


Figure 4.22: Strain data for FBGs (a) A, (b) B, (c) C, and (d) D for the undamaged specimen excited at 150 Hz.

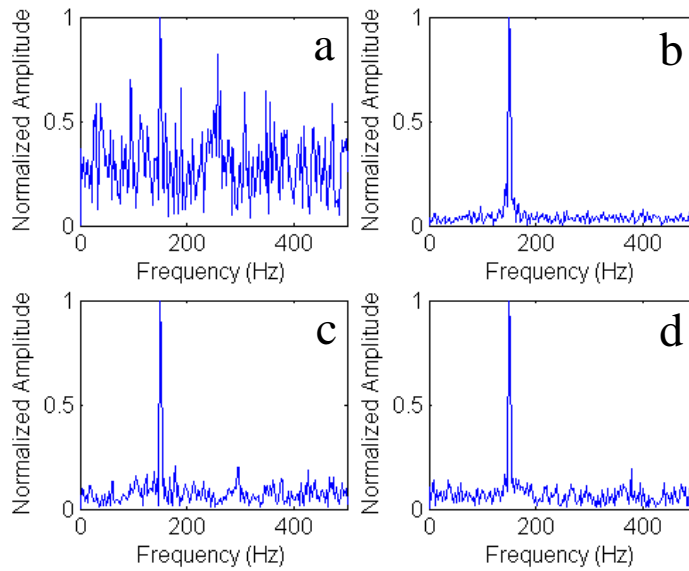


Figure 4.23: FFT results for FBGs (a) A, (b) B, (c) C, and (d) D for the undamaged specimen excited at 150 Hz.

Although the FFT gives an averaged-sense of the overall frequency components present in the dynamic signal, a short-time Fourier transform (STFT) can be used to see how the frequency components change with time. This information will yield insight as to whether transient behavior is present in the sensors' dynamic response. The STFT was calculated by discretizing the time signal into small windows of equal length, which are then used to calculate the FFT. For this study, all STFT calculations are performed with an 18 ms Hamming window and 50% overlap. These settings were determined through trial and error and best yielded a balance between time-scale resolution and accuracy in the FFT calculations. Additionally, all STFT calculations were plotted up to 1000 Hz because this was the range of the natural frequency testing performed. The resulting STFT plot for FBG B from the data in Figure 4.22(b) (undamaged, 150 Hz excitation) is shown in Figure 4.24. Contoured data plots were utilized to smooth window transitions. Note the distinct peak at 150 Hz throughout the duration of the signal. This result is expected for the undamaged specimen being driven at 150 Hz.

Figures 4.25 and 4.26 present the contoured STFT data calculated from each of the FBG sensors before damage was applied, and then after each impact. The intensity scales included for each plot are scaled to the values found in the undamaged case for that particular FBG. The units of these scales are arbitrary, so intensities cannot be reliably compared between FBGs; valid comparisons can only be made between plots of the same FBG.

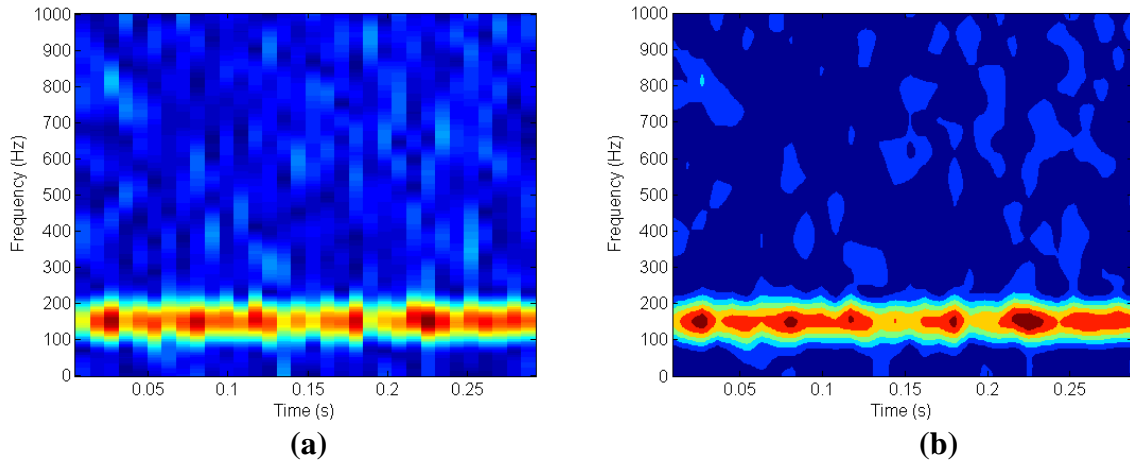
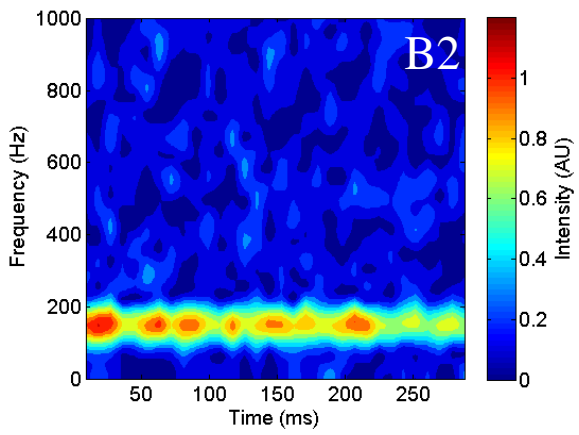
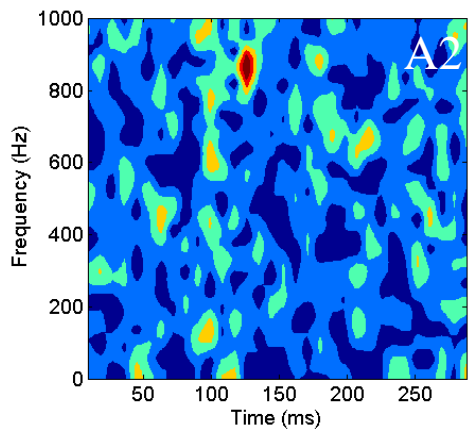
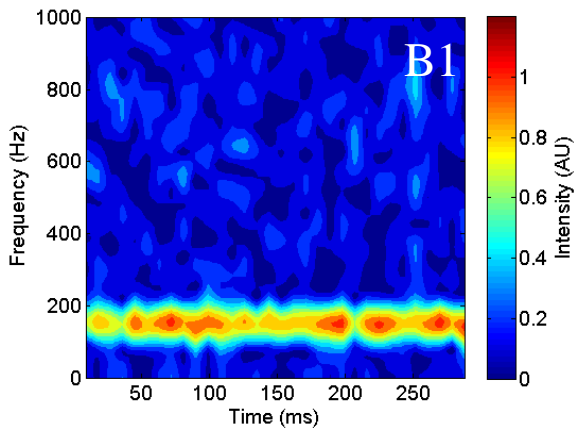
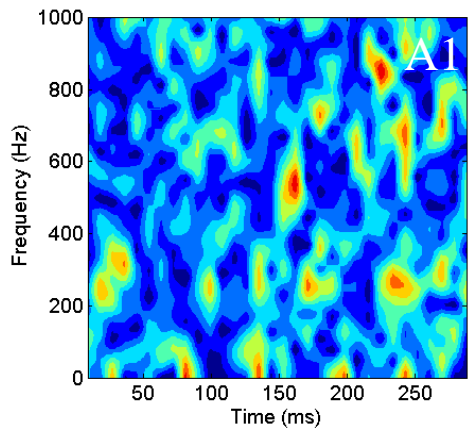
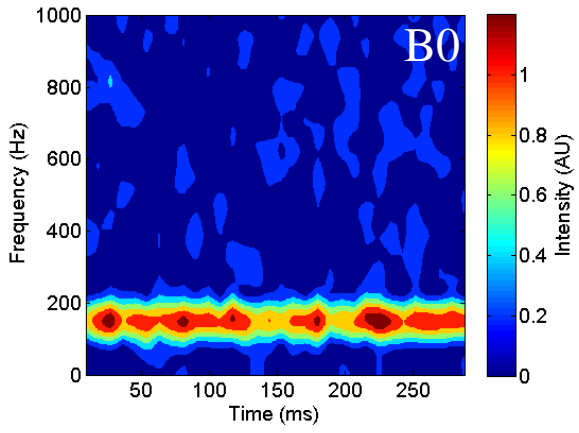
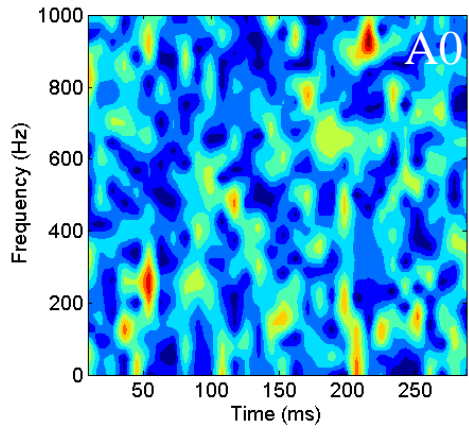


Figure 4.24: (a) Raw STFT data showing Hamming windows and (b) contoured STFT data for FBG B on the undamaged specimen excited at 150 Hz.

Figure 4.25: Contoured STFT data for FBG A (A) and FBG B (B) when (0) undamaged, and after (1) impact 1, (2) impact 2, (3) impact 3 and (4) impact 4. All data are at 150 Hz excitation frequency.



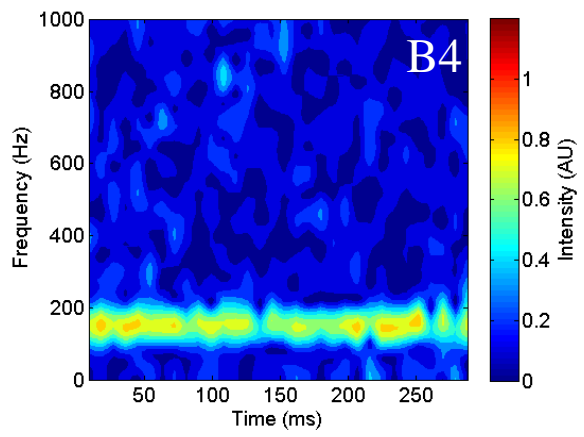
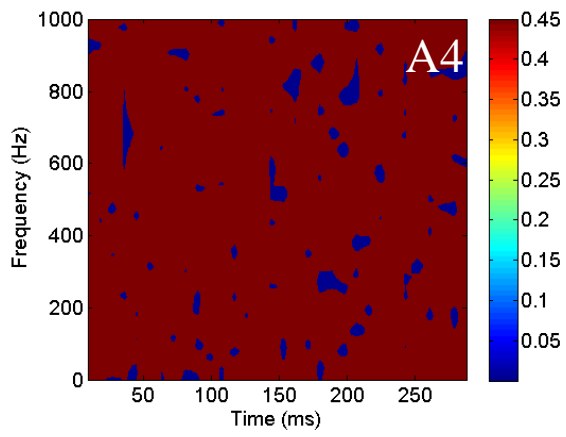
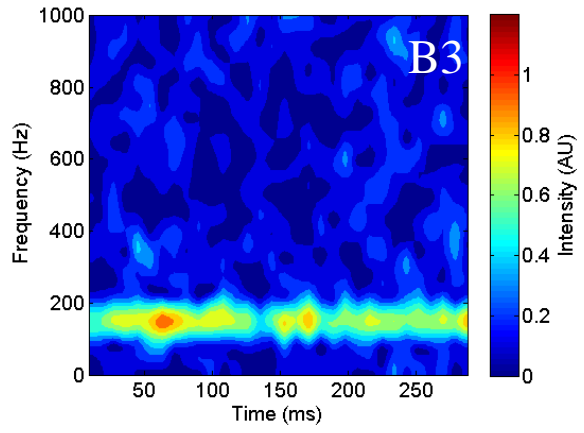
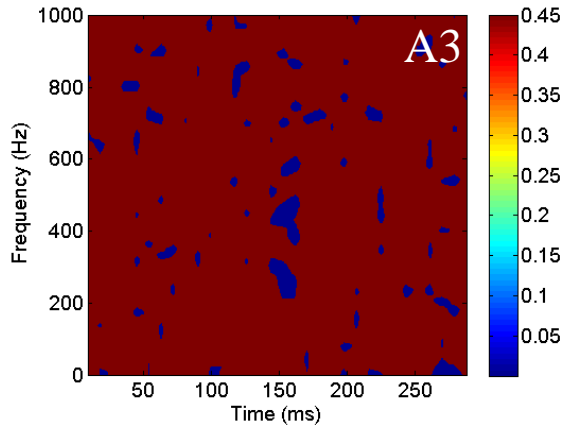
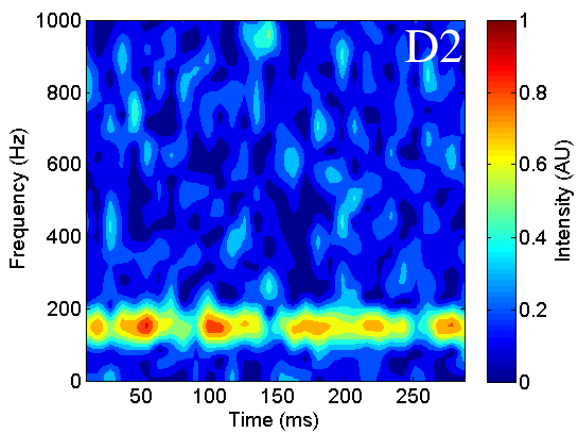
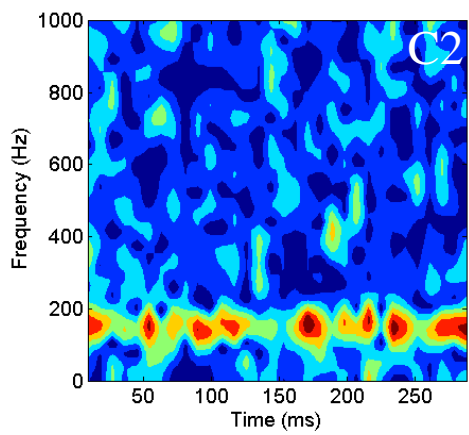
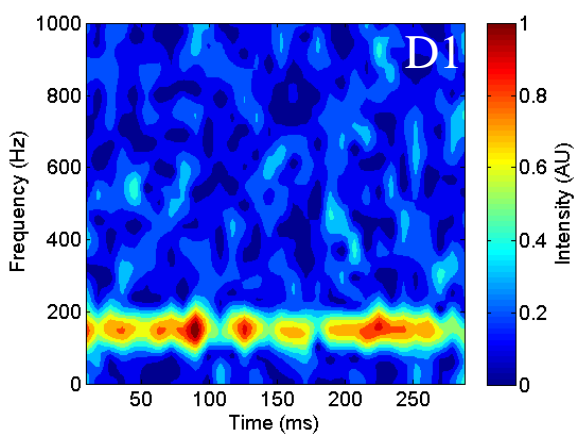
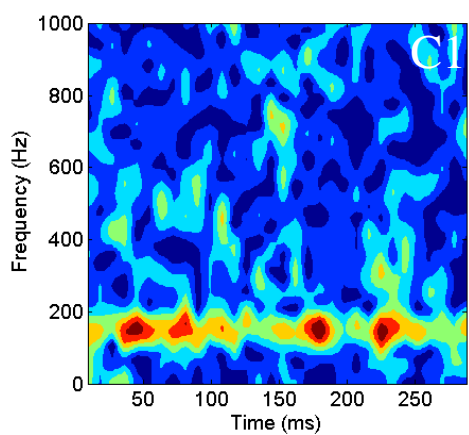
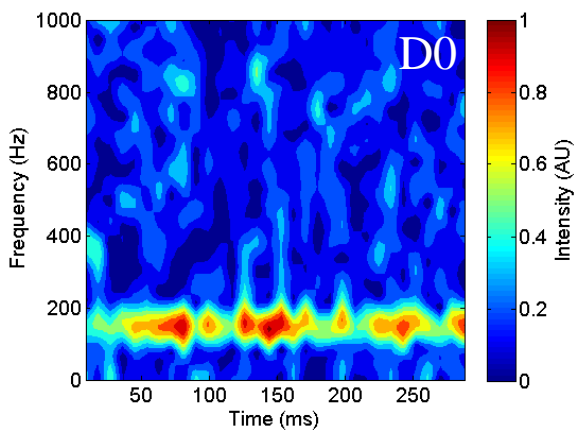
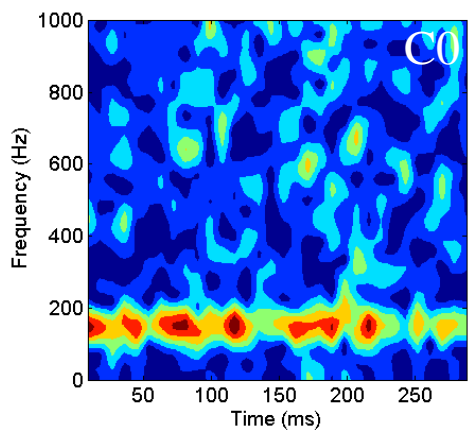
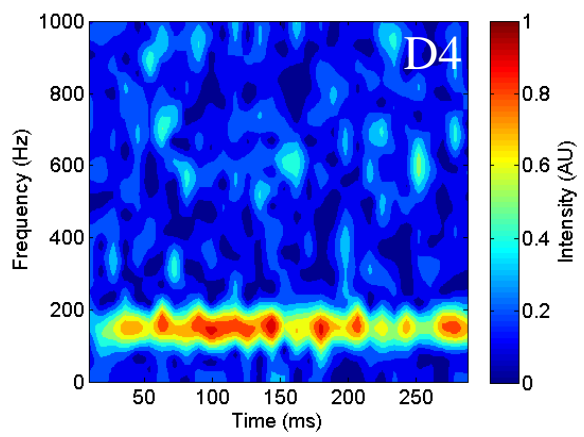
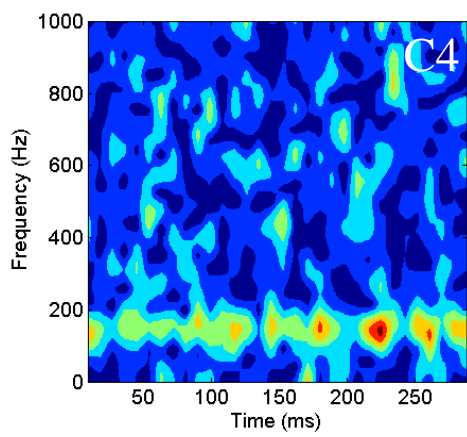
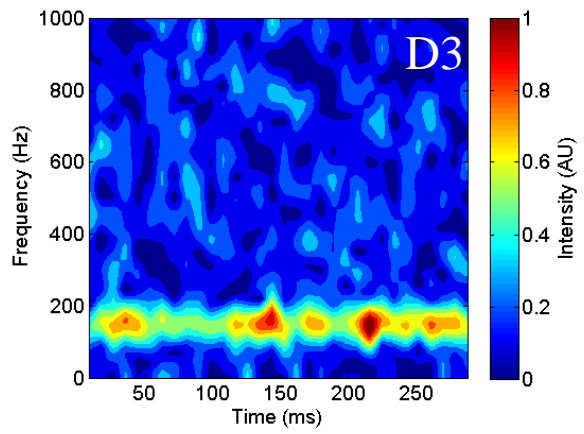
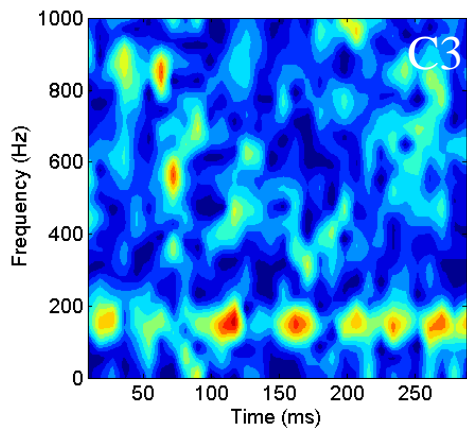


Figure 4.26: Contoured STFT data for FBG C (C) and FBG D (D) when (0) undamaged, and after (1) impact 1, (2) impact 2, (3) impact 3 and (4) impact 4. All data are at 150 Hz excitation frequency.





As discussed previously, FBG A was broken after impact 3. This is evident in the data of Figures 4.25(A3) and 5(A4), the measurements taken after the impact. Additionally, as discussed previously and shown in Figure 4.23, FBG A does not have a strong frequency response to the 150 Hz excitation when undamaged. This makes it difficult to use Figure 4.25(A0) as a reference state to compare the frequency response changes due to the impact events. Because Figure 4.25(A0) is inherently noisy, it is impossible to discern whether the changing frequency response shown in Figures 4.25(A1) and 4.25(A2) is in response to the impact damage, or whether it is just further manifestation of the noise. With this in mind, reliable conclusions cannot be drawn from the frequency response data for FBG A.

For the remaining FBG sensors, there are several features that suggest a transition from linear to nonlinear behavior. The first feature is the appearance and transient behavior of the resonant frequencies. In FBG B, the intensity of the 150 Hz component is strong and consistent across the acquisition time. But as damage progresses, the 150 Hz component becomes increasingly intermittent and significantly lower in intensity, while resonant frequencies begin to appear at higher frequencies. These resonant frequencies are more clearly seen if the color scale on Figure 4.25(B4) is reset to reflect the maximum values seen in the plot, as shown in Figure 4.27. While Figure 4.25(B4) hid some of these higher resonant frequencies, re-mapping the intensity spectrum reveals resonant frequencies appearing at 300 Hz, 450 Hz, 750 Hz, and 900 Hz.

This intermittent nature of the 150 Hz component as damage progresses can clearly be seen in FBG C as well, specifically in Figure 4.26(C3) and Figure 4.26(C4) when compared to the undamaged case in Figure 4.26(C0). Additionally, the development of

resonant frequencies can also be seen in FBG D in Figure 4.26(D4). Here, there are clear resonant frequencies developing at 300 Hz, 600 Hz, 750 Hz, and 900 Hz.

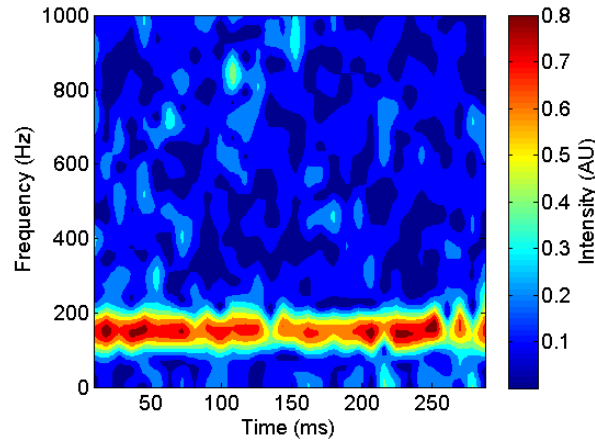


Figure 4.27: Contour plot for FBG B after impact 4, with color scale mapped to the max value on the plot.

The second feature to suggest nonlinear behavior is the appearance of sub-harmonics in the transient spectra; sub-harmonic components appear in the response of strongly nonlinear structures [13]. These sub-harmonics components are frequency components that occur below the primary driving frequency of 150 Hz. Although FBGs B and D have slight development of sub-harmonic components, FBG C clearly shows this trend. In the undamaged case (Figure 4.26(C0)), FBG C shows only a slight sub-harmonic at approximately 170 ms. As the damage to the specimen increases in Figures 4.26(C1) – 4.26(C4), the number and intensity of these sub harmonic increases, suggesting an increase in the nonlinear response of the specimen.

The final feature observed in nonlinear dynamic systems is a shift in the resonant frequencies of the system [14]. Although it is difficult to identify a shift in these frequencies in the data, there is a clear increase in bandwidth of the resonant frequencies in FBG C (Figures 4.26(C0) – 4.26 (C4)). This increase in bandwidth may be indicative of nonlinear behavior in the specimen's response.

These weak indications of nonlinear response are typical of the low sensitivity of data collected from surface mounted sensors, due to the transfer of strain through the strain gage adhesive. However, these data serve as an excellent benchmark for future tests with embedded sensors on similar specimens.

CHAPTER 5 – SIMULATIONS

5.1 MODELING DAMAGE

The goal of the simulations is to verify the results found experimentally. An emphasis was not placed on modeling the damages as accurately as possible; the development of accurate composite FEA representations of damage in laminated composites is the goal of many other studies, but is not the focus of this work. This study is concerned with predicting the changes that occur in the transient response as damage is introduced, not reproducing the exact same strain results. Therefore, damage was introduced into the model by reducing the elastic moduli of those elements that fell within the damaged regions around an impact location. Modeling the damage in this manner will not yield identical strain values to an experimental study, but should be sufficient to identify changes in transient behavior.

Specific damage region shapes and sizes were defined by the micro-CT images found in Figures 4.15 and 4.16. Figure 5.1 depicts the finite element model, with the damaged regions highlighted in green. The yellow regions denote the locations of FBG sensors and will be the elements used to extract transient information. Due to the large computational time, the simulation was only run for the undamaged and post-impact 4 cases.

To simulate damage, the Young's modulus and shear modulus for the elements within the damaged regions were set to be nearly zero [15]. These values could not be set exactly to zero because it would cause a singularity in the FEA calculation. These properties therefore were set at the following values:

$$E_x = E_y = E_z = 100 \text{ Pa}$$

$$G_{xy} = G_{yz} = G_{xz} = 50 \text{ Pa}$$

These property values relate to a decrease in strength from the pristine structure by a factor of 10^8 , which makes them effectively act as zero.

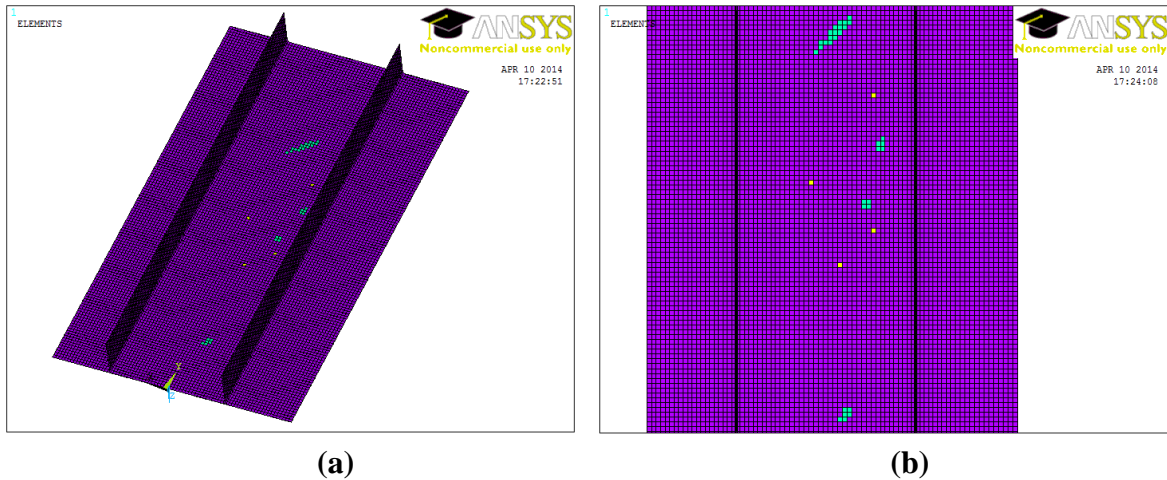


Figure 5.1: Damage (green) and FBG (yellow) locations within the FEA model for the (a) whole model and in (b) a detailed view.

5.2 TRANSIENT FORCE APPLICATION

With the model geometry fully defined in Chapter 3 and damage specifications described above, the only remaining component for the simulation is the applied loading. In this case, the loading was input as a transient force defined by the motion of the vibration table. The accelerometer was mounted directly to the vibration table, which was driven at an excitation frequency of 150 Hz at $6 V_{pp}$ (matching the experimental loading case). This voltage vs. time output data was recorded and converted to force vs. time data using the

manufacturers specified conversion ratio of 0.0980 (m/s²)/mV and the accelerometer's mass of 7.8 g. This force vs. time plot is shown in Figure 5.2, along with the associated FFT plot. Note the FFT shows a clear driving signal at 150 Hz, along with minor harmonics at much lower amplitude. This signal was matched using a Sum of Sines fit as shown in Figure 5.3, and corresponding to the equation

$$f = \sum_{n=1}^N A_n * \sin(B_n x + C_n) \quad (3)$$

However, only the first sine wave ($n = 1$) had non-negligible coefficients, so the final fit was $A_1 = 0.3644$, $B_1 = 942.4$, and $C_1 = 0.05296$. Equation (3) was deemed a good fit with $R^2 = 0.9939$. Using the same boundary conditions discussed in Section 4.2 for natural frequency testing, the transient forcing function was applied transversely across the model, as shown in Figure 5.4, for both the undamaged and damaged cases. All transient simulations were performed for a total run-time of 150 ms, with a step size of 0.35 ms. At each sensor location, the normal strain component in the direction of the FBG sensor was extracted from the model at each time step. The same processing as for the experimental measurements (FFT, STFT) was then applied to these simulated FBG measurements.

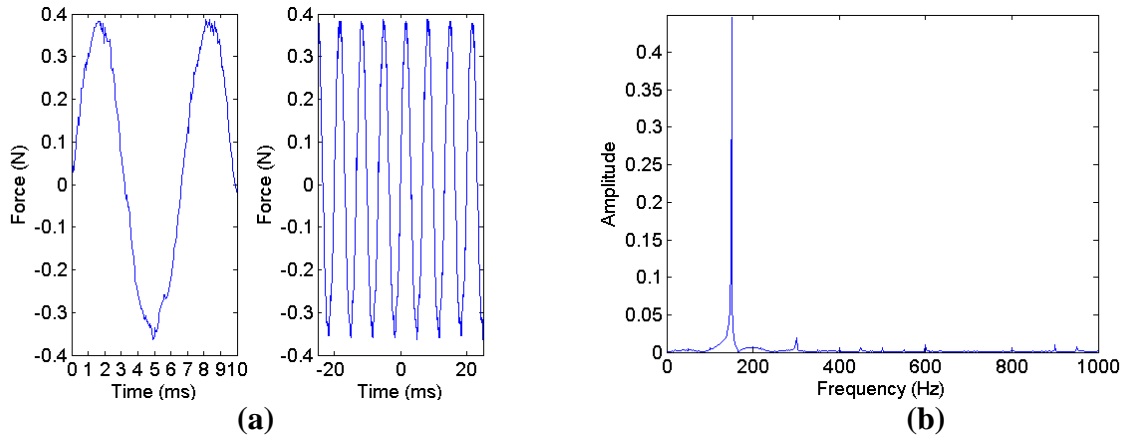


Figure 5.2: (a) Force vs. time plot for vibration table transient force and (b) associated FFT plot.

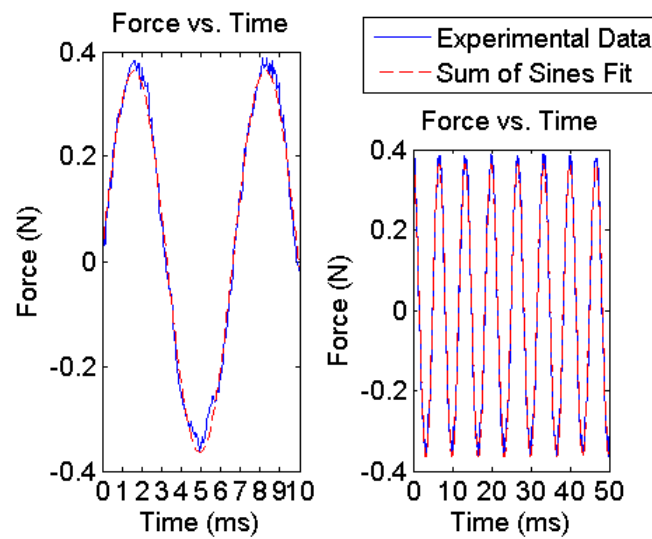


Figure 5.3: Sum of sines fit for transient input force.

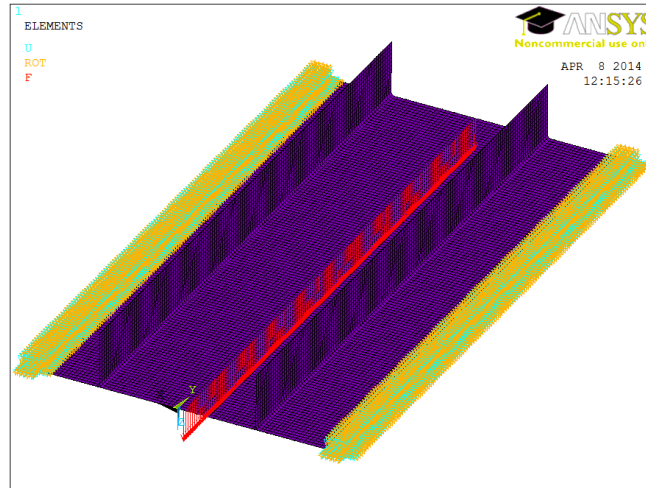


Figure 5.4: Loading case for simulated harmonic excitation.

5.3 MODEL SIMULATION RESULTS

The damage applied to the model, based on the shape of the damage seen in the micro-CT images, yielded very little change in the predicted transient response of the stiffened panel, as seen by comparing Figures 5.6(a) and 5.6(b). The experimental data showed the development of harmonics as the level of damage increased, but this trend was not present in the simulation results. There are thought to be two reasons for this discrepancy. The first source is the “perfect” nature of the boundary conditions and the structure in the model. While the experimental specimen certainly contains many minor flaws (hollow cavities, non-consistent fiber density, etc.), the simulated specimen contains none of these manufacturing flaws. These minor defects create harmonics in the frequency response of the experimental specimen, and account for such harmonics showing up in the experimental data. With that said, these components were very weak in the experimental results, suggesting the

damage only caused minor changes in the appearance of these harmonics. Additionally, the boundary conditions in the experimental model may damp out some of the frequency response of the stiffened panel, as they are not truly rigid.

The second potential source of the low level of response changes observed in the model is the accuracy of the damage reconstruction from the micro-CT images. Before damage was applied, it was expected that the damaged regions would be larger than those identified by the micro-CT scan. The micro-CT images shown in Figures 4.15 and 4.16 are taken perpendicular to the plane of impact, thus showing the propagation of the damage shape. Although taking the images in this orientation shows perfectly the shape of the impact, it has the potential to miss other aspects of laminate failure, specifically delamination. Delamination would occur parallel to the micro-CT scan planes, and thus be overlooked. Due to time constraints, it was not possible to fully analyze the micro-CT reconstruction in this MS project, as this was not the focus of this work. Future work will further analyze the micro-CT data. Considering the pre-impact expectation of damage propagation, a second damage-case simulation was run using the expected damage size, as shown in Figure 5.5(c). This model used the same reduced material properties given earlier, merely expanding the size of the damage regions. The size of these damage regions was based on the resulting damages seen in the experiment. Impact 2 yielded the largest damage area, and was made a square damage region encompassing the initially modeled damage region. The other damage regions were estimations in size; they are modeled smaller than the Impact 2 region, but larger than their respective initial damage model size.

The transient results of this expected damage case are shown in Figure 5.6(c). In this damage case, there is a much more significant change in the transient results. In this case, the main frequency component at 150 Hz in FBG A and FBG C became more consistent over time. We still do not see a significant change in the higher frequency responses in the STFT plots, though some slight changes can be identified around 500 Hz in the FFT plots shown in Figure 5.7. These small changes offer further support for the minor changes seen in the experimental results when consideration is again given to the perfect model boundary conditions.

At this point it is also worth noting the significant frequency response at 61.4 Hz seen in FBGs B and D. This response is shown clearly in the FFT plot for these FBGs, as shown in Figure 5.7. This component is also present in FBGs A and C, but remains lower in intensity than the main 150 Hz component. This frequency component coincides very closely to the predicted natural frequency of the model at 60.6 Hz. The 150 Hz driving frequency may be activating this mode at 60.6 Hz at a high level of intensity in the numerical model. With this new data, the sub-harmonics identified in the experimental results are worth revisiting. Some of these sub-harmonics could actually be similar manifestations of this ~61 Hz natural frequency, though they are activated at a lower intensity than is seen in the model. However, the irregularity of the sub-harmonics seen in Figures 4.25 and 2.26 make it difficult to know the exact source of these measured frequencies. Embedding sensors within the specimen may provide a better understanding of this 61.4 Hz component. For the numerical model, this 61.4 Hz frequency component is also likely influencing the frequency changes seen around 500 Hz; while the undamaged case contains a response at 530 Hz, after

the expected damage is applied, this response shifts to 491.6 Hz, a harmonic of the lower order 61.4 Hz component.

The final point worth noting is the drastic reduction in the 150 Hz component in FBG D once the damage was applied. This is particularly visible in the FFT plot for FBG D in Figure 5.7. This drastic change is likely seen only in FBG D because it is the only FBG that has its strain measurement lined up directly with a damage location. While the other FBGs had the damage applied above or below their strain measurement orientation, FBG D has a damage location directly in line with its strain measurement (x -direction). This close proximity to a location of effectively zero load transfer capability would have drastic effects on the transient response of the FBG, which seems to manifest as a significant reduction in the 150 Hz component.

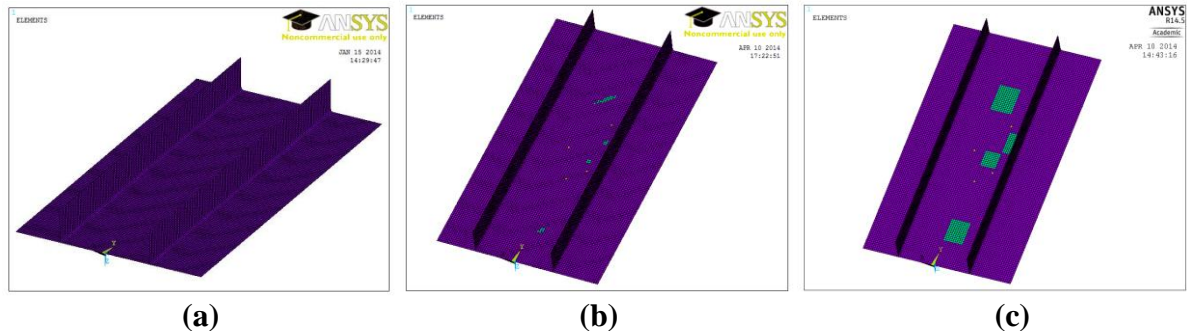


Figure 5.5: (a) Undamaged model, (b) model with damage shape based on micro-CT scans, and (c) model with expected damage regions. Green area is damage region.

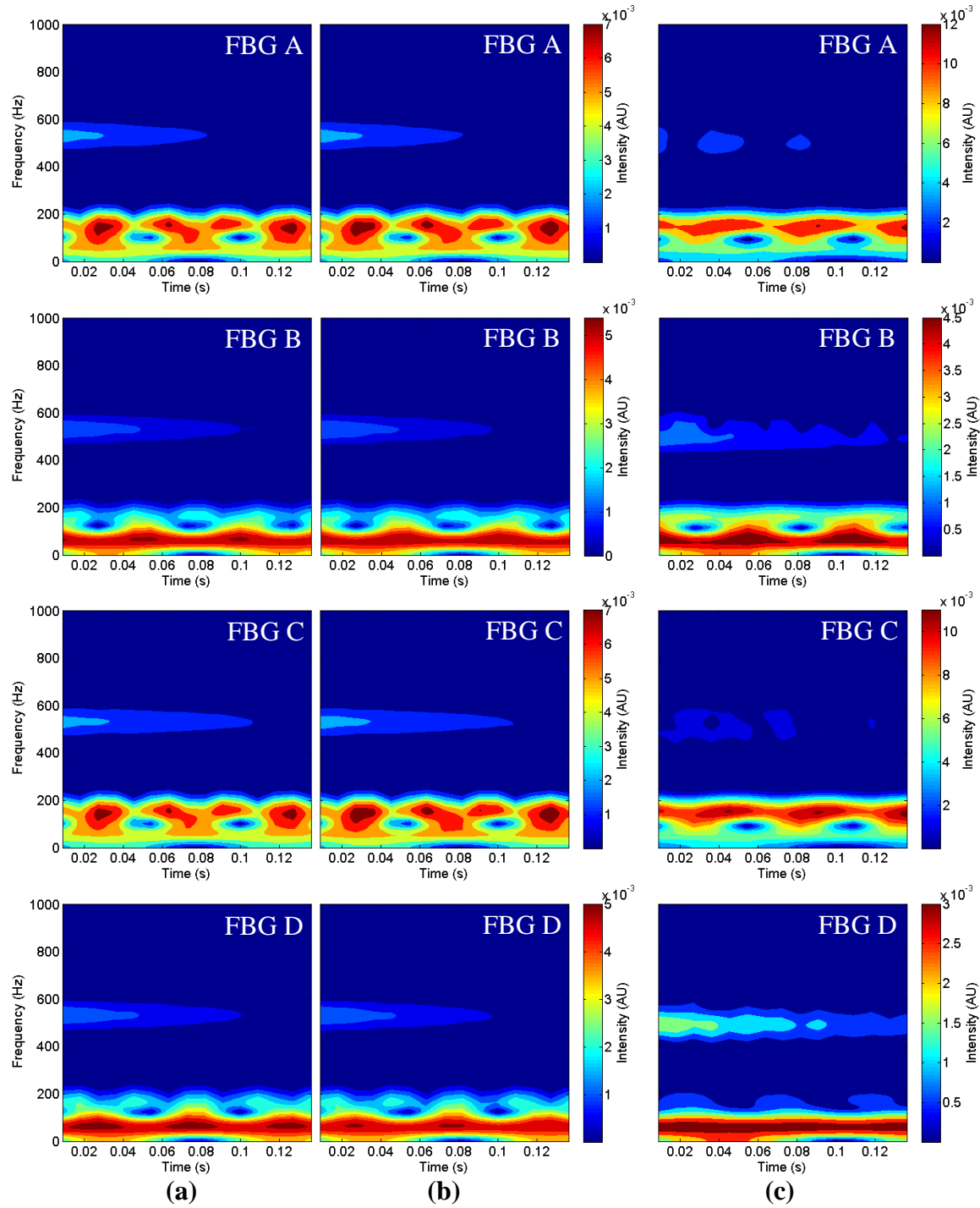


Figure 5.6: STFT for model results. (a) Left column is undamaged case, (b) middle is micro-CT scan damage shape case, and (c) right is expected damage case. Note intensity scales vary.

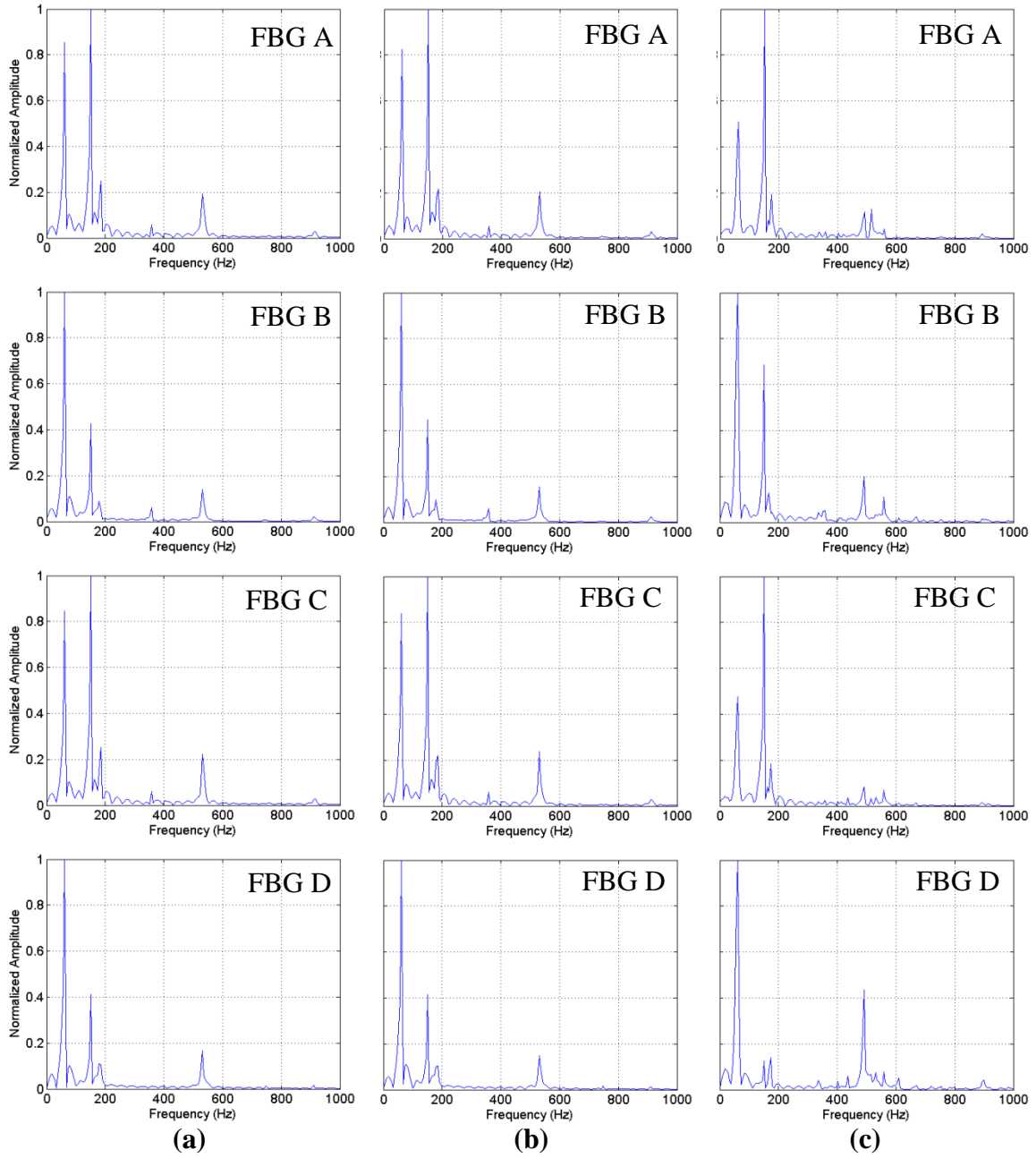


Figure 5.7: FFT for model results. (a) Left column is undamaged case, (b) middle is micro-CT scan damage shape case, and (c) right is expected damage case.

CHAPTER 7 - CONCLUSION

7.1 CONSLUSIONS

The outcome of this work was the demonstration of the measurement of dynamic responses in a complex, stiffened panel composite structure using surface mounted FBGs. The measurements were performed using full-spectral interrogation to eliminate peak wavelength errors due to spectral distortion and will be used as benchmark data for comparison with embedded FBG sensor measurements at a later date. To obtain these measurements, several research accomplishments were achieved.

The development of a VARTM manufacturing process for high quality, integrally stiffened panel specimens was successful. Through many trial-and-error attempts, a process for manufacturing an integrally stiffened panel was laid out. In a parallel project, the same procedure was followed by another researcher to produce an integrally stiffened panel of similar dimensions and quality. The development of a numerical model to simulate the undamaged specimen was also successful. The model fit to the specimen was assessed by the correlation of experimental natural frequencies to those found through simulation. Eight of the eleven first natural frequencies found experimentally were identified closely by the numerical model, with the differences in results being accounted for by mode shape capture issues. This correlation in natural frequencies through the first 11 modes offered cleared evidence of a well-fit model and the high quality of the specimen fabrication. The applied

boundary conditions damped out some natural frequencies more than others, however this is expected with physical systems.

Using a high speed, full spectral interrogator, the FBG sensors were able to clearly depict the transient response of the integrally stiffened panel subjected to harmonic excitation. Additionally, the surface mounted FBG sensors demonstrated an ability to sense minor changes in the transient response, and identified several trends that may be indicative of non-linear response in the specimen. Though these trends were not extremely strong, they do offer promising results for the potential use of FBG sensors as real-time structural health monitoring devices in aircraft. The limited sensitivity of the sensors to the changes in transient response may be a result of surface mounting the sensors. If the sensors were embedded within the carbon fiber panel, they would likely be much more sensitive to these changes and potentially offer more distinct indications of a transition to non-linear response in the panel. It should also be noted that while not the focus of this work, the dynamic response of multiple multiplexed FBG sensors were measured through high-speed, full-spectral interrogation for the first time.

The simulation of damage in the specimen offered mixed results. While the limited change in transient response as damaged was applied did support the only minor changes seen in the experimental results, it was expected to see more evolution in the transient response. Exploring the theory that the initial damage regions identified by the Micro-CT scan were conservative, the follow-up simulation using larger expected damage regions showed much greater change in the transient response of the simulated panel, though the appearance of harmonics was still notably absent. It is believed that the perfect nature of the

model and the applied boundary conditions limited the appearance of these harmonic components.

7.2 FUTURE WORK

Based on these results, a few areas of focus for future work are recommended to further quantify the ability of FBG sensors to identify changes in the dynamic response of damaged stiffened panels:

1. Embedding of sensors within an identical, integrally stiffened panel and repeating the vibration testing sequence with and without impact damage will permit the comparison between surface mounted and embedded FBG sensitivity to damage. Although the exact form of impact damage cannot be replicated in these specimens, similar general trends can be evaluated. It is expected that embedding the FBG sensors would drastically increase the sensitivity of the sensors, and potentially offer more obvious changes in the transient response of the specimen as damage progresses.
2. Based on the results of the model, it seems that more investigation is needed as to how to properly assess the size and shape of the damage region found using the Micro-CT scanning technique. Accurate modeling of this damage size and shape is necessary to use the numerical model as a supporting case for experimental results.

REFERENCES

- [1] Webb, S., Peters, K., Zikry, M., Vella, T., Chadderdon, S., Selfridge, R. , & Schultz, S. (2011). Wavelength hopping due to spectral distortion in dynamic fiber bragg grating sensor measurements. *Measurement Science and Technology*, 22(6), 065301.
- [2] Takeda, N., Okabe, Y., & Mizutani, T. (2007). Damage detection in composites using optical fibre sensors. *Journal of Aerospace Engineering*, 221(4), 497-508.
- [3] Takeda, S.-, Aoki, Y., & Nagao, Y. (2012). Damage monitoring of CFRP stiffened panels under compressive load using FBG sensors. *Composite Structures*, 94(3), 813-819.
- [4] Vella, T., Chadderdon, S., Selfridge, R., Schultz, S., Webb, S., Park, C., Peters, K., Zikry, M. (2010). Full-spectrum interrogation of fiber bragg gratings at 100 khz for detection of impact loading. *Measurement Science and Technology*, 21, 094009.
- [5] Webb, S., Peters, K., Zikry, M., Chadderdon, S., Stan, N., Selfridge, R. , & Schultz, S. (2013). Full-spectral interrogation of fiber bragg grating sensors exposed to steady-state vibration. *Experimental Mechanics*, 53, 513-530.
- [6] Webb, S., Shin, P., Peters, K., Zikry, M., Stan, N., Chadderdon, S., Selfridge, R., Schultz, S. (2014). Characterization of fatigue damage in adhesively bonded lap joints through dynamic, fullspectral interrogation of fiber bragg grating sensors: 1. experiments. *Smart Materials and Structures*, 23, 025016.
- [7] Webb, S., Shin, P., Peters, K., Zikry, M., Stan, N., Chadderdon, S., Selfridge, R., Schultz, S. (2014). Characterization of fatigue damage in adhesively bonded lap joints through dynamic, fullspectral interrogation of fiber bragg grating sensors: 2. simulations. *Smart Materials and Structures*, 23, 025017.
- [8] Huang, C. (2003). Study on co-cured composite panels with blade-shaped stiffeners. *Composites Part A: Applied Science and Manufacturing*, 34(5), 403-410.
- [9] Soller Composites. (2012). Unidirectional carbon fiber fabric. Retrieved from Soller Composites: Your Leading Edge Composite Supplier website: <http://www.sollercomposites.com/>
- [10] Daniel, I. M., & Ishai, O. (2006). Properties of typical unidirectional composites (two-dimensional). In *Engineering mechanics of composite materials* (p. 377). New York: Oxford University Press.

- [11] ACP Composites. (2012). Mechanical properties of carbon fiber composite materials. Retrieved from ACP Composites website:
<http://www.acpsales.com/upload/Mechanical-Properties-of-Carbon-Fiber-Composite-Materials.pdf>
- [12] Hill, K. O., & Meltz, G. (1997). Fiber bragg grating technology fundamentals and overview. *Journal of Lightwave Technology*, 15(8), 1263-1276.
- [13] Carpinteri, A., & Pugno, N. (2005). Towards chaos in vibrating structures-part 1: Theory and period doubling cascade. *Journal of Applied Mechanics*, 72, 511-518.
- [14] Touzé, C., Thomas, O., & Amabili, M. (2011). Transition to chaotic vibrations for harmonically forces perfect and imperfect circular plates. *International Journal of Non-Linear Mechanics*, 46, 234-246.
- [15] Wenk, J. F. (2003). A Finite Element Analysis of Damage Accumulation in Heterogenous Structures (Master's thesis). Retrieved from
https://engineering.purdue.edu/FEND2/student_resources/BSME_Thesis_JFW.pdf

APPENDICES

APPENDIX A – VARTM PROCESS

Detailed layup process for producing the specimen used in this study.



Figure A.1: Completed VARTM assembly.

1. Stiffener layup process:

- a. Coat inside surfaces of metal molds with 2 layers of car wax
- b. Using 90° angle channel aluminum, lay up the mold in the following manner:

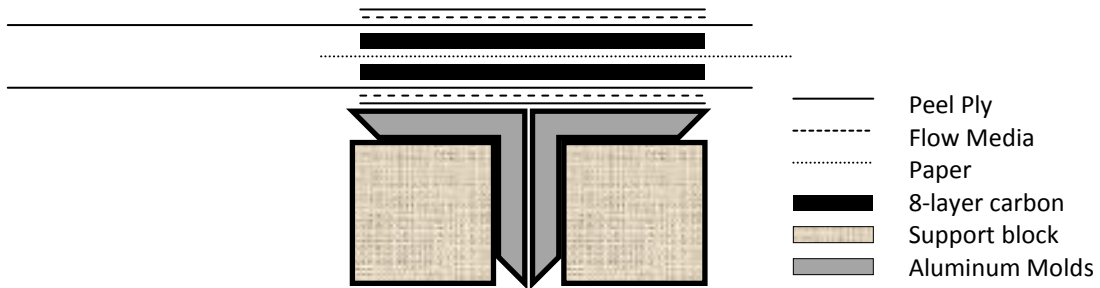


Figure A.2: Stiffener layup.

- i. Carbon layers – Consists of two sets of 8-layer layups with the stacking sequence +45/-45/0/90/90/0/-45/+45 for each set
- ii. Peel Ply layers
 - 1. Two pieces cut to the same size as the inside surface of the mold (the inside surfaces are those surfaces that will touch the layup)
 - 2. Two pieces cut much larger than the aluminum molds
- iii. Flow Media layers – Two pieces cut to the same size as the inside surface of the mold
- iv. Paper – Thin sheet of paper used to mark the middle of the mold. Will be removed before infusion.
- v. The support blocks are present merely to facilitate the layup process. They allow the molds to lay flat while the pieces are laid down.
- c. Clamp the mold together (until vacuum bag is placed)
 - i. Add another aluminum mold on top of layup and clamp together (see arrows)

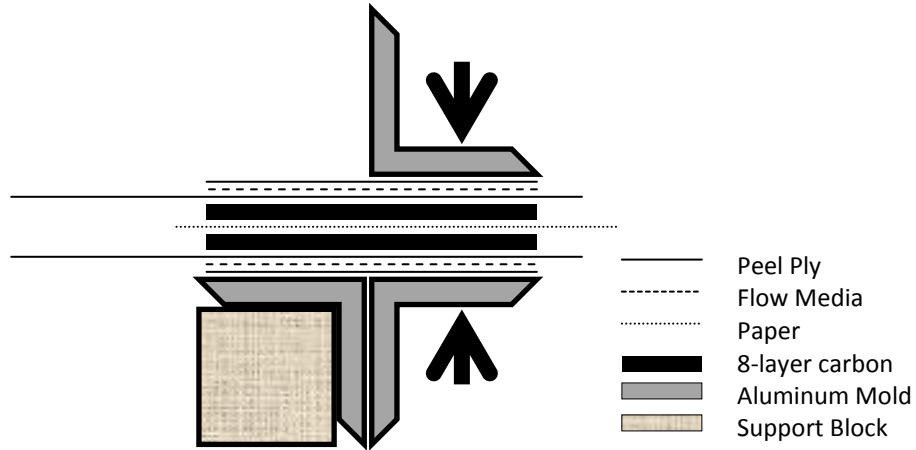


Figure A.3: Stiffener clamping procedure.

- ii. Fold down peel ply extending from top of layup and tape (painters blue tape) to mold surface
- iii. Wrap a piece of tape (painters blue tape) around each end of the mold
- iv. Remove the extra aluminum mold and support block

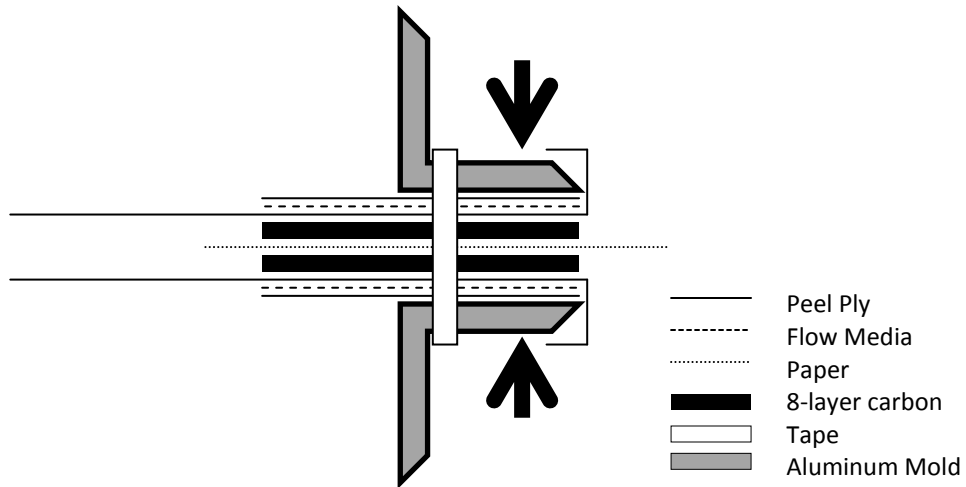


Figure A.4: Completed stiffener mold.

- d. Repeat this process for the other stiffener
2. Clean working table
 - a. Scrape any resin, debris, tape, etc. from the table surface
 - b. Use a small amount of adhesive remover to clean the table surface
3. Panel layup process:
 - a. Lay down a piece of release film slightly larger than the carbon panel size
 - b. Lay down 8 layers of carbon fiber panels in proper stacking sequence
 - c. Place stiffener molds in desired location on top of panel
 - i. Use the paper in the middle of the mold to know where to split the carbon fiber
 - ii. Once the molds are placed, CAREFULLY pull out the paper from the top (the molds are still clamped at this point, and may need to be loosened to remove the paper)
 - iii. The peel ply extending from the mold should cover the whole panel preform
 - iv. Leave the clamps on the mold until the vacuum bag is placed over top (later step)
 - d. Place strips of flow media over the panel in the areas not covered by the stiffener molds (these are big enough to cover the panel, but not extend off of it or overlap the molds)
 - e. Final layup cross section view:

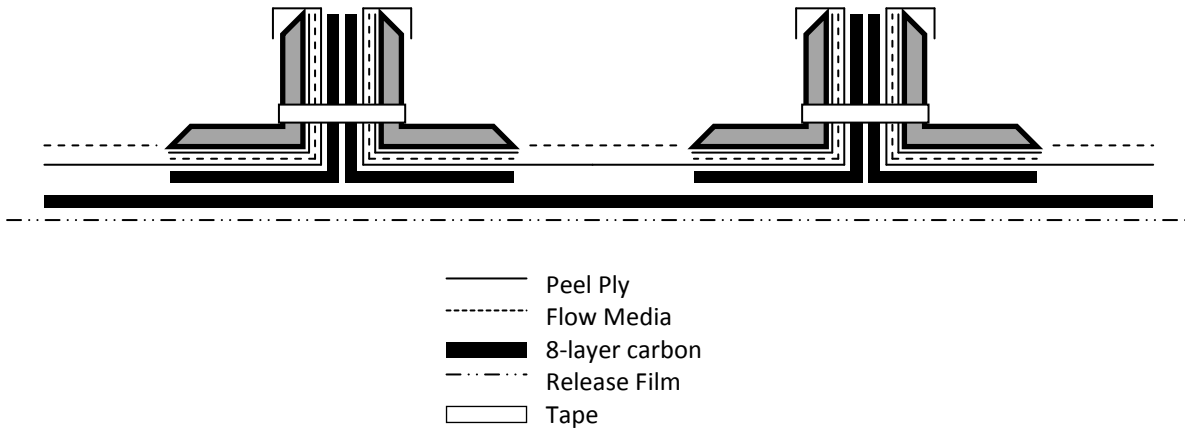


Figure A.5: Cross-section of mold lay up.

4. Set up vacuum system

a. Lay down tacky-tape around the panel layup

- i. Tacky tape is actually a kind of putty. It comes in a roll that can be cut into strips, hence it being called “tape.” Once off the rolled, it can be manipulated like putty.
- ii. Leave AT LEAST 6 cm between the perform and tacky tape on the ends
- iii. Leave about 3 cm between the preform and tacky tape on the sides
- iv. Overlap tape in corners
- v. Diagram:

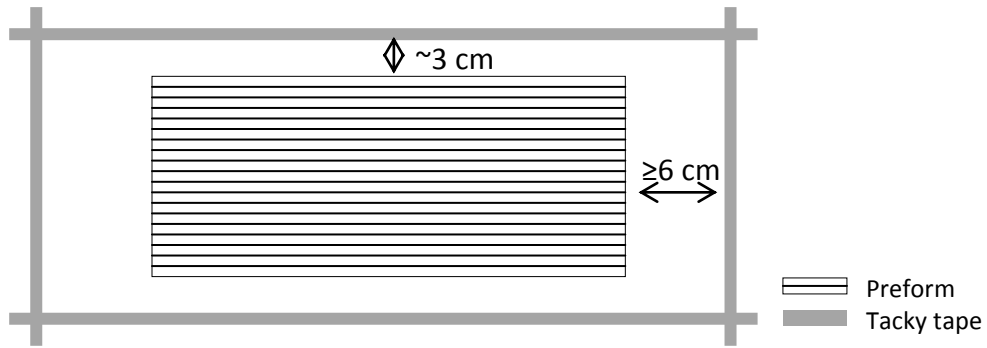


Figure A.6: Vacuum seal spacing.

b. Create tubing inlet and outlet systems

i. Connect tubing system

1. Put spiral tube into the rigid tube
2. Put rigid tube into the large flexible tube
3. Put small flexible tube into other end of large flexible tube
4. Wrap all joints (except spiral tube – rigid tube joint) in tacky-tape to create air-tight seals

5. Diagram:

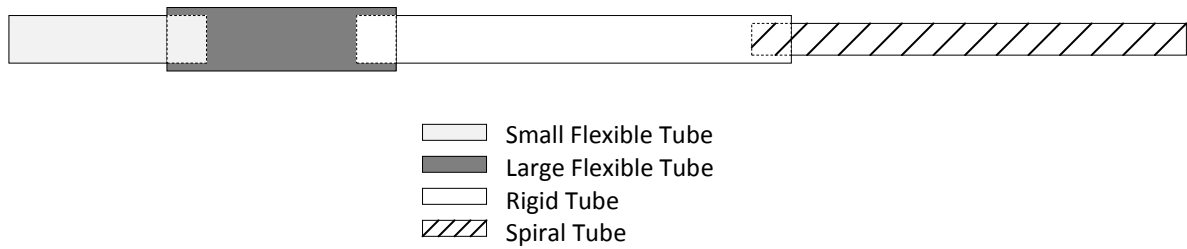


Figure A.7: Inlet/outlet tube connection diagram.

6. Put a circle of tacky-tape around the middle of the rigid tube.

This will be used to help make a tight air seal.

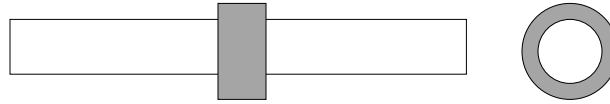


Figure A.8: Inlet/outlet tube vacuum seal.

7. Do this process twice (once for inlet and once for outlet)
- ii. Connect the tubing systems to the vacuum setup
 1. Lay a strip of peel ply along the length of both sides of the preform (use a small amount of blue painter's tape to connect the peel ply to the table if desired)
 2. Lay the tube systems on top of these peel ply strips
 - a. Spiral tube should run the length of the preform and extend slightly past on both ends. Do NOT stretch the spiral tube far (just enough tension to keep the tube straight).
 - b. Use a small amount of tacky-tape to connect the end of the spiral tube to the table.
 - c. The circle of tacky tape on the rigid tube should align with the tacky tape laid around the preform.
 - d. Diagram:

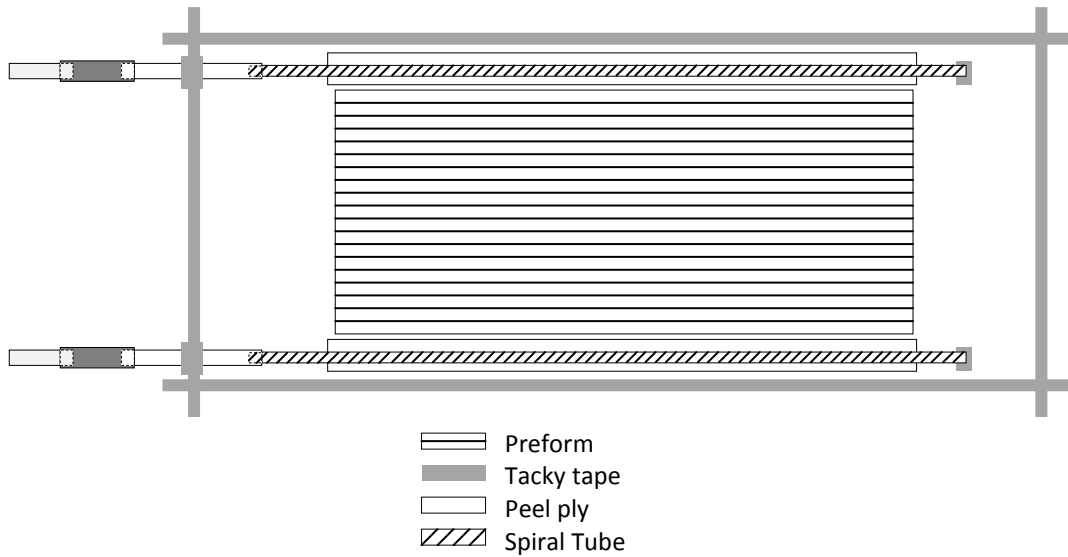


Figure A.9: Vacuum seal layout.

- e. One of the small flexible tubes will then connect to the vacuum, while the other will be placed into the resin source. It does not matter which one.
- iii. Build a tacky tape “bridge” over rigid tubes
 1. Use tacky tape to create a connection for vacuum bag over the flexible tubes. We already put a wrap of tape around the tube, but more tape will be needed because the vacuum bag cannot reach into tight corners.
 2. A suggested method for creating this bridge is to put rolls of tacky tape into the corners, and then put strips of it over the top (cross section of bridge below). Then press down into tape to

remove ALL air pockets; the removal of these air pockets is crucial.



Figure A.10: Initial vacuum seal around inlet/outlet tubes.

3. Ultimately, the cross section of the bridge of the tubes should look something like this:

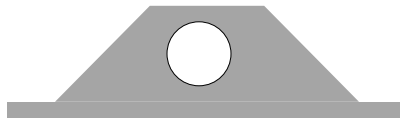


Figure A.11: Final vacuum seal around inlet/outlet tubes.

- c. Apply vacuum bag
 - i. Remove the clamps from the stiffener molds.
 - ii. Be sure to cut the vacuum bag larger than the area surrounded by the tacky tape.
 - iii. The vacuum bag must be applied while under tension (i.e. no slack in the bag when it is connected).

- iv. It is recommended to attach the bag on two opposite corners (under slight tension), and then connect around all edges while pulling the bag tight.
 - 1. All that is needed for attaching the bag to the tacky tape is a slight press of the bag to the tacky tape.
 - 2. Once the bag is connected all the way around, go back and press firmly down into the bag—tacky tape connection.
- v. Crimp all edges of the tacky tape
 - 1. Use a thin tool (we use the narrow edge of a paint stir stick) to press down on all edges of the tacky tape through the vacuum bag. This step is crucial in ensuring an airtight seal. See diagram of tacky tape cross section before and after crimping:

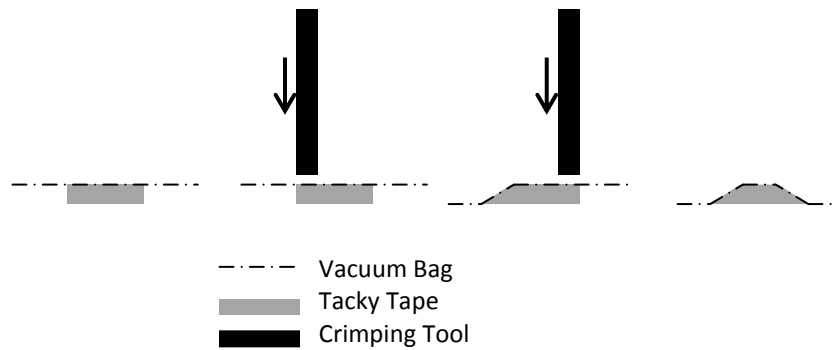


Figure A.12: Crimping procedure for vacuum seal.

- 5. Vacuum check
 - a. Connect the outlet tube to the vacuum and clamp the inlet tube shut.

- b. Turn on the vacuum and check for leaks.
 - i. Leaks can often times be found by listening for air escaping.
 - ii. If there are no audible leaks, connect a pressure gauge to the inlet tube.
Now, release the clamp on the inlet tube, then clamp the outlet tube (going to the vacuum). If there are no leaks, the pressure gauge should maintain a constant reading (around 1044 psi in our case). If the pressure gauge begins to drop, there is a leak in the vacuum seal somewhere in the vacuum system that needs to be sealed.
- c. Once it has been verified that there are no leaks present, clamp both the inlet and outlet and leave the set up for at least 24 hours. If the pressure has remained constant when you return, you can be sure that there are no leaks in the system.

6. Resin infusion

- a. Mix the epoxy and hardener, and then place in a vacuum chamber to de-gas for 25 minutes.
- b. Place the inlet tube in the resin bucket and release clamps on inlet and outlet.
- c. Turn on vacuum and allow resin to travel through entire preform.
- d. Once the entire preform is wet (can be visually checked), clamp the resin inlet and allow any excess resin that has built up near the inlet tube to be pulled into the preform.
- e. Once there is no longer any resin built up near the inlet, clamp the outlet tube and turn off the vacuum.

- f. Allow the mold to sit for about 48 hours, or as per epoxy instructions
7. Removal from mold
- a. Remove vacuum bag and surrounding tacky tape from table, leaving just the panel layup and molds
 - b. Pull off blue tape that was used to hold down the peel ply protruding from the top of the mold
 - c. With tape removed, pull this flap of peel ply away from the mold

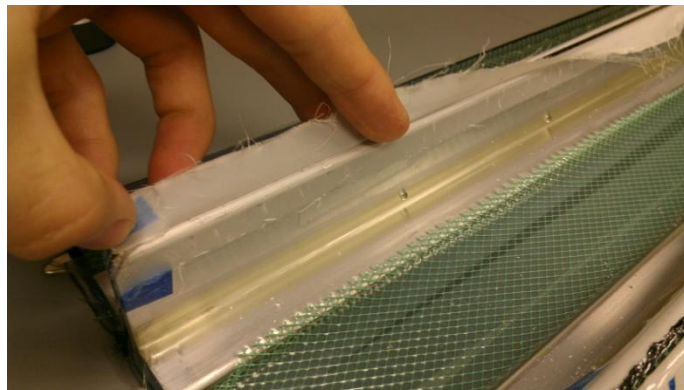


Figure A.13: Peel ply used for removing stiffener molds.

- d. Now use a putty knife to wedge between this flap of peel ply and the metal mold. It is recommended that you start in the corner of the mold. It is crucial that you use the spatula at this location because it will keep you from scratching the panel. Slowly work your way along the length of the mold until it releases.

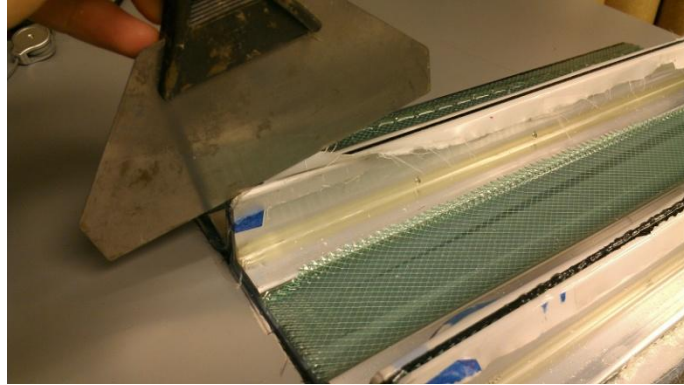


Figure A.14: Putty knife used to remove stiffener molds.

- e. Use the exposed peel ply to pull the remaining peel ply away from the panel.
 - i. Because this peel ply is located beneath the flow media, removing it will also remove the flow media.
- f. Repeat for all 4 mold pieces